



1 A simple topography-driven and 2 calibration-free runoff generation module

3 Hongkai Gao^{1,2,3*}, Christian Birkel^{4,5}, Markus Hrachowitz⁶, Doerthe Tetzlaff⁵, Chris Soulsby⁵, Hubert H. G. Savenije⁶

4

5 ¹ Key Laboratory of Geographic Information Science (Ministry of Education of China), East China Normal University,
6 Shanghai, China.

7 ² School of Geographical Sciences, East China Normal University, Shanghai, China.

8 ³ Julie Ann Wrigley Global Institute of Sustainability, Arizona State University PO Box 875402. Tempe, AZ 85287-5402.

9 ⁴ Department of Geography, University of Costa Rica, San José, Costa Rica

10 ⁵ Northern Rivers Institute, University of Aberdeen, Scotland.

11 ⁶ Water Resources Section, Delft University of Technology, Delft, Netherlands.

12

13 *Corresponding to Hongkai Gao (hkgao@geo.ecnu.edu.cn)

14

15 Abstract

16 Reading landscapes and developing calibration-free runoff generation models that adequately reflect land
17 surface heterogeneities remains the focus of much hydrological research. In this study, we report a novel
18 and simple topography-driven runoff generation parameterization – the HAND-based Storage Capacity
19 curve (HSC), that uses a topographic index (HAND, Height Above the Nearest Drainage) to identify
20 hydrological similarity and the extent of saturated areas in catchments. The HSC can be used as a module
21 in any conceptual rainfall-runoff model. Further, coupling the HSC parameterization with the Mass Curve
22 Technique (MCT) to estimate root zone storage capacity (S_{uMax}), we developed a calibration-free runoff
23 generation module HSC-MCT. The runoff generation modules of HBV and TOPMODEL were used for
24 comparison purposes. The performance of these two modules (HSC and HSC-MCT) was first checked
25 against the data-rich Bruntland Burn (BB) catchment in Scotland, which has a long time series of field-
26 mapped saturation area extent. We found that the HSC performed better in reproducing the spatio-
27 temporal pattern of the observed saturated areas in the BB compared to TOPMODEL. The HSC and HSC-
28 MCT modules were subsequently tested for 323 MOPEX catchments in the US, with diverse climate, soil,



29 vegetation and geological characteristics. Comparing with HBV and TOPMODEL, the HSC performs better
30 in both calibration and validation. Despite having no calibrated parameters, the HSC-MCT module
31 performed comparably well with calibrated modules, highlighting the robustness of the HSC
32 parameterization to describe the spatial distribution of the root zone storage capacity and the efficiency
33 of the MCT method to estimate S_{uMax} . Moreover, the HSC-MCT module facilitated effective visualization
34 of the saturated area, which has the potential to be used for broader hydrological, ecological,
35 climatological, geomorphological, and biogeochemical studies.

36

37 1 Introduction

38 Determining the volume and timing of runoff generation from rainfall inputs remains a central challenge
39 in rainfall-runoff modelling (Beven, 2012; McDonnell, 2013). Creating a simple, calibration-free, but robust
40 runoff generation module has been, and continues to be, an essential pursuit of hydrological modellers.
41 Although we have made tremendous advances to enhance our ability on Prediction in Ungauged Basins
42 (PUB) (Hrachowitz et al., 2013), it is not uncommon that models become increasingly complicated in order
43 to capture the details of hydrological processes shown by empirical studies (McDonnell, 2007; Sivapalan,
44 2009). More detailed process conceptualization normally demands higher data requirements than our
45 standard climatological and hydrological networks can provide, leading to more calibrated parameters
46 and a probable increase in model uncertainty (Sivapalan, 2009).

47 Hydrological connectivity is a key characteristic of catchment functioning, controlling runoff generation.
48 It is a property emerging at larger scales, describing the temporal dynamics of how spatially
49 heterogeneous storage thresholds in different parts of catchments are exceeded to contribute to storm
50 runoff generation and how they are thus “connected to the stream” (e.g. Zehe and Blöschl, 2004;
51 Bracken and Croke, 2007; Lehmann et al., 2007; Zehe and Sivapalan, 2009; Ali et al., 2013; Blume and
52 van Meerveld, 2015). Connectivity is controlled by a multitude of factors (Ali and Roy, 2010), including
53 but not limited to surface (e.g. Jencso et al., 2009) and subsurface topography (e.g. Tromp-van Meerveld
54 and McDonnell, 2006), soils (including preferential flow networks; e.g. Zehe et al., 2006; Weiler and
55 McDonnell, 2007) and land cover (e.g. Imeson and Prinsen, 2004; Jencso and McGlynn, 2011; Emanuel
56 et al., 2014) but also by the wetness state of the system (e.g. Detty and McGuire, 2010; Penna et al.,
57 2011; McMillan et al., 2014; Nippgen et al., 2015).



58 In detailed distributed hydrological bottom-up models, connectivity emerges from the interplay of
59 topography, soil type and water table depth. For example, TOPMODEL (Beven and Kirkby, 1979; Beven
60 and Freer, 2001) uses topographic information to distinguish hydrologic similarity; and SHE (Abbott et al.
61 1986) and tRIBS (Ivanov et al. 2004; Vivoni et al. 2005) use partial differential equations to describe the
62 water movement based on pressure gradients obtained by topography; and the Representative
63 Elementary Watershed (REW) approach divides catchment into a number of REWs to build balance and
64 constitutive equations for hydrological simulation (Reggiani et al., 1999; Zhang and Savenije, 2005; Tian
65 et al., 2008). As the relevant model parameters such as local topographic slope and hydraulic
66 conductivity can, in spite of several unresolved issues for example relating to the differences in the
67 observation and modelling scales (e.g. Beven, 1989; Zehe et al., 2014), be obtained from direct
68 observations, they could *in principle* be applied without calibration.

69 Zooming out to the macro-scale, top-down models, in contrast, are based on emergent functional
70 relationships that integrate system-internal heterogeneity (Sivapalan, 2005). These functional
71 relationships require parameters that are effective on the modelling scale and that can largely not be
72 directly determined with small-scale field observations (cf. Beven, 1995). Parameters in these models
73 are therefore traditionally determined by calibration. However, frequently the number of observed
74 variables for model calibration is, if available at all, limited to time series of stream flow. The absence of
75 more variables to constrain models results in such models being ill-posed inverse problems. Equifinality
76 in parameterization and in the choice of parameters then results in considerable model uncertainty (e.g.
77 Beven, 1993, 2006). To limit this problem and to also allow predictions in the vast majority of
78 catchments worldwide that remain ungauged it is therefore desirable to find ways to directly infer
79 effective model parameters at the modelling scale from readily available data (Hrachowitz et al., 2013).

80 The component that is central for establishing connectivity in most top-down models is the soil moisture
81 routine. Briefly, it controls the dynamics of water storage and release in the unsaturated root zone and
82 partitions water into evaporative fluxes, groundwater recharge and fast lateral, storm flow generating
83 runoff. The latter of which is critical from the aspect of connectivity. In regions where Hortonian
84 overland flow (i.e. infiltration excess overland flow) is of minor importance, the term fast lateral flows
85 can represent, depending on the model and the area of application, different processes, such as
86 saturation overland flow, preferential flow, flow through shallow, high permeability soil layers or
87 combinations thereof. The interplay between water volumes that are stored and those that are released
88 laterally to the stream via fast, connected flow paths (“connectivity”) is in most top-down models



89 described by functions between water stored in the unsaturated root zone (“soil moisture”) and the
90 areal proportion of heterogeneous, local storage thresholds that are exceeded and thus “connected”
91 (Zhao et al., 1980). In other words, in those parts of a catchment where the storage threshold is
92 exceeded, no more additional water can be stored and additional water input in these parts of the
93 catchment will generate fast, lateral flows. This areal proportion of the catchment where thresholds are
94 exceed can alternatively be interpreted as runoff coefficient (e.g. Ponce and Hawkins, 1996; Perrin and
95 Andreassian, 2001; Fenicia et al., 2007; Bergström and Lindström, 2015). The idea goes back to the
96 variable contributing area concept, assuming that only partial areas of a catchment, where soils are
97 saturated and thus storage thresholds are exceeded, contribute to runoff (Hewlett, 1961; Dunne and
98 Black, 1970; Hewlett and Troendle, 1975). Although originally developed for catchments dominated by
99 saturation overland flow, the extension of the concept to subsurface connectivity, posing that surface
100 and subsurface connectivity are “two sides of the same coin” (McDonnell, 2013), proved highly valuable
101 for models such as Xinanjiang (Zhao et al., 1980), HBV (Bergström and Forsman, 1973; Bergström and
102 Lindström, 2015), SCS-CN (Ponce and Hawkins, 1996; Bartlett et al., 2016), FLEX (Fenicia et al., 2008) or
103 GR4J (Perrin and Andreassian et al., 2001), applied in other regions, too.

104 The parameters of these storage excess distribution functions are typically calibrated. In spite of being
105 the core component of soil moisture routines in many top-down models, little effort was previously
106 invested to find ways to determine the shape of the functions describing the spatial heterogeneity of
107 storage thresholds and thus connectivity pattern at the catchment-scale directly from available data. An
108 important step towards understanding and quantifying connectivity pattern directly based on
109 observations was recently achieved by intensive experimental work in the Tenderfoot Creek catchments
110 in Montana, US. In their work Jencso et al. (2009) were able to show that connectivity of individual
111 hillslopes in their headwater catchments is highly related to their respective upslope accumulated areas.
112 Using this close relationship, Smith et al. (2013) successfully developed a simple top-down model with
113 very limited need for calibration, emphasizing the value of “enforcing field-based limits on model
114 parameters” (Smith et al., 2016). Based on hydrological landscape analysis, Savenije (2010) suggested
115 that as topographical features are frequently linked to distinct hydrological functional traits, they may
116 potentially be used to construct a conceptual catchment model based on a perceptual model of
117 hydrological units. Gharari et al., 2014 found that by imposing semi-quantitative relational constraints,
118 the FLEX-Topo model can dramatically reduce the need for calibration. The model has also shown to
119 hold considerable potential for spatial model transferability without the need for parameter re-
120 calibration (Gao et al., 2014a; H. Gao et al., 2016).



121 In many top-down models, such as Xinanjiang or HBV, connectivity is formulated in a general form as
122 $C_R=f(S_U(t),S_{uMax},\beta)$, where C_R is the runoff coefficient, i.e. the proportion of the catchment generating
123 runoff, $S_U(t)$ is the catchment water content in the unsaturated root zone at any time t , S_{uMax} is a scale
124 parameter representing the total storage capacity in the unsaturated root zone and β is a shape
125 parameter, representing the spatial distribution of heterogeneous storage capacities in the unsaturated
126 root zone. In a recent development, several studies suggest that S_{uMax} can be robustly and directly
127 inferred long term water balance data, by the Mass Curve Technique (MCT), without the need for
128 further calibration (Gao et al., 2014; de Boer-Euser et al., 2016; Nijzink et al., 2016). This leaves shape
129 parameter β as only free calibration parameter for soil moisture routines of that form.

130 Topography is often the dominant driver of water movement caused by prevailing hydraulic gradients.
131 More crucially, topography usually provides an integrating indicator for hydrological behavior, since
132 topography is usually closely related with other landscape elements, such as soil vegetation climate and
133 even geology (Seibert et al., 2007; Savenije, 2010; Rempe and Dietrich, 2014; Gao et al., 2014b; Maxwell
134 and Condon, 2016; Gomes, 2016). The Height Above the Nearest Drainage (HAND; Rennó et al., 2008;
135 Nobre et al., 2011; Gharari et al., 2011), which can be computed from readily available digital elevation
136 models, could potentially provide first order estimates of groundwater depth, as there is some
137 experimental evidence that with increasing HAND, groundwater depths similarly increase (e.g. Haria and
138 Shand, 2004; Martin et al., 2004; Molenat et al., 2005, 2008; Shand et al., 2005; Condon and Maxwell,
139 2015; Maxwell and Condon, 2016). HAND can be interpreted as a proxy of the hydraulic head and is thus
140 potentially more hydrologically informative than the topographic elevation above sea level (Nobre et al.,
141 2011). Compared with the Topographic Wetness Index (TWI) in TOPMODEL, HAND is an explicit measure
142 of a physical feature linking terrain to water relative to the potential energy for local drainage (Nobre et
143 al., 2011). More interestingly, topographic structure emerges as a powerful force determining rooting
144 depth under a given climate or within a biome, revealed by ecological observations in global scale (Fan
145 et al., 2017). This leads us to think from ecological perspective to use the topographic information as an
146 indicator for root zone spatial distribution without calibrating the β , and coupling it with the MCT
147 method to estimate the S_{uMax} , eventually create a calibration-free runoff generation module.

148 In this study we are therefore going to test the hypotheses that: (1) HAND can be linked to the spatial
149 distribution of storage capacities (β) and therefore can be used to develop a new runoff generation
150 module; (2) the distribution of storage capacities determined by HAND contains different information
151 than the topographic wetness index; (3) the estimates of β together with water balance-based estimates



152 of S_{uMax} allow the formulation of calibration-free parameterizations of soil moisture routines in top-down
153 models directly based on observations. All these hypotheses will be tested firstly in a small data-rich
154 experimental catchment (the Bruntland Burn catchment in Scotland), and then apply the model to a wide
155 range of larger catchments (MOPEX, Model Parameter Estimation Experiment).

156 This paper is structured as follows. In the Methods section, we describe two of our proposed modules, i.e.
157 HSC (HAND-based Storage Capacity curve) and HSC-MCT, and two benchmark models (HBV, TOPMODEL).
158 This section also includes the description of other modules (i.e. interception, evaporation and routing) in
159 rainfall-runoff modelling, and the methods for model evaluation, calibration and validation. The Dataset
160 section reviews the empirically-based knowledge of the Bruntland Burn catchment in Scotland and the
161 hydrometeorological and topographic datasets of MOPEX catchments in the US for model comparison. The
162 Results section presents the model comparison results. The Discussion section interprets the relation
163 between rainfall-runoff processes and topography, catchment heterogeneity and simple model, and the
164 implications and limitations of our proposed modules. The conclusions are briefly reviewed in the
165 Summary and Conclusions section.

166 2 Methods

167 Based on our perceptual model that SEF is the dominant runoff generation mechanism in most cases, we
168 developed the HAND-based Storage Capacity curve (HSC) module. Subsequently, estimating the
169 parameter of root zone storage capacity (S_{uMax}) by the Mass Curve Techniques (MCT) without calibration,
170 the HSC-MCT was developed. In order to assess the performance of our proposed modules, two widely-
171 used runoff generation modules, i.e. HBV power function and TOPMODEL module, were set as
172 benchmarks. Other modules, i.e. interception, evaporation and routing, are kept with identical structure
173 and parameterization for the four rainfall-runoff models (HBV, TOPMODEL, HSC, HSC-MCT, whose names
174 are from their runoff generation modules), to independently diagnose the difference among runoff
175 generation modules (Clark et al., 2008; 2010).

176 2.1 Two benchmark modules

177 HBV power function

178 The HBV runoff generation module applies an empirical power function to estimate the nonlinear
179 relationship between the runoff coefficient and soil moisture (Bergström and Forsman, 1973; Bergström
180 and Lindström, 2015). The function is written as:



$$181 \quad A_s = \left(\frac{S_u}{S_{uMax}} \right)^\beta \quad (1)$$

182 Where A_s (-) represents the contributing area, which equals to the runoff coefficient of a certain rainfall
 183 event; S_u (mm) represents the averaged root zone soil moisture; S_{uMax} (mm) is the averaged root zone
 184 storage capacity of the studied catchment; β (-) is the parameter determining the shape of the power
 185 function. The prior range of β can be from 0.1 to 5. The $S_u - A_s$ has a linear relation while β equals to 1. And
 186 the shape becomes convex while the β is less than 1, and the shape turns to concave while the β is larger
 187 than 1. In most situations, S_{uMax} and β are two free parameters, cannot be directly measured at the
 188 catchment scale, and need to be calibrated based on observed rainfall-runoff data.

189 **TOPMODEL module**

190 The TOPMODEL assumes topographic information captures the runoff generation heterogeneity at
 191 catchment scale, and the TWI is used as an index to identify rainfall-runoff similarity (Beven and Kirkby,
 192 1979; Sivapalan et al., 1997). Areas with similar TWI values are regarded as possessing equal runoff
 193 generation potential. More specifically, the areas with larger TWI values tend to be saturated first and
 194 contribute to SEF; but the areas with lower TWI values need more water to reach saturation and generate
 195 runoff. The equations are written as follow:

$$196 \quad D_i = \bar{D} + S_{uMax} (\overline{I_{TW}} - I_{TW_i}) \quad (2)$$

$$197 \quad \bar{D} = S_{uMax} - S_u \quad (3)$$

$$198 \quad A_s = \sum A_{s_i}; \quad \text{while } D_i < 0 \quad (4)$$

199 Where D_i (mm) is the local storage deficit below saturation at specific location (i); \bar{D} (mm) is the averaged
 200 water deficit of the entire catchment (Equation 2), which equals to $(S_{uMax} - S_u)$, as shown in Equation 3. I_{TW_i}
 201 is the local I_{TW} value. $\overline{I_{TW}}$ is the averaged TWI of the entire catchment. Equation 2 means in a certain soil
 202 moisture deficit condition for the entire catchment (\bar{D}), the soil moisture deficit of a specific location (D_i),
 203 is determined by the catchment topography (I_{TW} and I_{TW_i}), and the root zone storage capacity (S_{uMax}).
 204 Therefore, the areas with D_i less than zero are the saturated areas (A_{s_i}), equal to the contributing areas.
 205 The integration of the A_{s_i} areas (A_s), as presented in Equation 4, is the runoff contributing area, which
 206 equals to the runoff coefficient of that rainfall event.



207 Besides continuous rainfall-runoff calculation, Equations 2-4 also allow us to obtain the contributing area
208 (A_s) from the estimated relative soil moisture (S_u/S_{uMax}), and then map it back to the original TWI map,
209 which makes it possible to test the simulated contributing area by field measurement. It is worth
210 mentioning that the TOPMODEL in this study is a simplified version, and not identical to the original one,
211 which combines the saturated and unsaturated soil components.

212 2.2 HSC module

213 Hydrological models are human constructs that simplify the larger reality of hydrological processes
214 (Savenije, 2009), and assumptions are inevitable (Neuweiler and Helmig, 2017). In this study, we assume
215 1) SEF is the dominant runoff generation mechanism, while SOF and SSF cannot be distinguished; 2) the
216 local root zone storage capacity has a positive and linear relationship with HAND, from which we can
217 derive the spatial distribution of the root zone storage capacity; 3) HAND contours are parallel to each
218 other in runoff generation. We believe that rainfall firstly feeds local soil moisture deficit, and no runoff
219 can be generated before areas being subsequently saturated and water moving downslope. And after
220 being saturated and connected with the channel network, either the cascade or parallel model structure
221 does not impact on runoff generation. So this parallel model structure not only simplifies our simulation,
222 it is also very likely closer to reality (Savenije, 2010).

223 Figure 1 shows the perceptual HSC module, in which we simplified the complicated 3-D topography of a
224 real catchment into a 2-D simplified hillslope. And then derive the distribution of root zone storage
225 capacity, based on topographic analysis and the second assumption as mentioned in the preceding
226 paragraph. Figure 2 shows the approach to derive the S_u - A_s relation, which are detailed as follows.

- 227 I. **Generate HAND map.** The HAND map of study catchment can be generated from Digital Elevation
228 Model (DEM) (Gharari et al., 2011). The stream initiation threshold area is a crucial parameter,
229 determining the perennial river channel network (Montgomery and Dietrich, 1989; Hooshyar et
230 al., 2016), and significantly impacting the HAND values.
- 231 II. **Generate normalized HAND distribution curve.** Firstly, sort the HAND values of grid cells in
232 ascending order. Secondly, the sorted HAND values were evenly divided into n bands (e.g. 20
233 bands in this study), to make sure each HAND band has similar area. The averaged HAND value of
234 each band is regarded as the HAND value of that band. Thirdly, normalize the HAND bands, and
235 then plot the normalized HAND distribution curve (Figure 1b).
- 236 III. **Distribute S_{uMax} to each HAND band (S_{uMax_i}).** As assumed, the normalized storage capacity of each
237 HAND band (S_{uMax_i}) increases with HAND value (Figure 1c). Based on this assumption, the



238 unsaturated root zone storage capacity (S_{uMax}) can be distributed to each HAND band as S_{uMax_i}
 239 (Figure 2a). It is worth noting that S_{uMax} needs to be calibrated in the HSC module, but free of
 240 calibration in the HSC-MCT module.

241 IV. **Derive the S_u - A_s curve.** With the number of s saturated HAND bands (Figure 2a-c), the soil
 242 moisture (S_u) can be obtained by Equation 5; and saturated area proportion (A_s) can be obtained
 243 by Equation 6.

$$244 \quad S_u = \frac{1}{n} [\sum_{i=1}^s S_{uMax_i} + S_{uMax_s}(n - s)] \quad (5)$$

$$245 \quad A_s = \frac{s}{n} \quad (6)$$

246 Where S_{uMax_s} is the maximum S_{uMax_i} of all the saturated HAND bands. Subsequently, the A_s - S_u
 247 curve can be derived, and shown in Figure 2d.

248 The SEF mechanism assumes that only the saturated areas generate runoff, therefore the proportion of
 249 saturation area is equal to the runoff coefficient of that rainfall-runoff event. Based on the S_u - A_s curve in
 250 Figure 2d, generated runoff can be calculated from root zone moisture (S_u). The HSC module also allows
 251 us to map out the fluctuation of saturated areas by the simulated catchment average soil moisture. For
 252 each time step, the module can generate the simulated root zone moisture for the entire basin (S_u). Based
 253 on the S_u - A_s relationship (Figure 2d), we can map S_u back to the saturated area proportion (A_s) and then
 254 visualize it in the original HAND map. Based on this conceptual model, we developed the computer
 255 program and created a procedural module. The technical roadmap can be found in Figure 3.

256 2.3 HSC-MCT module

257 The S_{uMax} is an essential parameter in various hydrological models (e.g. HBV, Xinanjiang, GR4J), which
 258 determines the long-term partitioning of rainfall into infiltration and runoff. Gao et al., 2014a found that
 259 S_{uMax} represents the adaption of ecosystems to local climate. Ecosystems may design their S_{uMax} based on
 260 the precipitation pattern and its water demand. The storage is neither too small to avoid mortality in dry
 261 seasons, nor too large to consume excessive energy and nutrients. Based on this assumption, we can
 262 estimate the S_{uMax} without calibration, by the MCT method, from climatological and vegetation
 263 information. More specifically, the average annual plant water demand in the dry season (S_R) is
 264 determined by the water balance and the vegetation phenology, i.e. precipitation, runoff and seasonal
 265 NDVI. Subsequently, based on the annual S_R , the Gumbel distribution (Gumbel, 1935), frequently used for
 266 estimating hydrological extremes, was used to standardize the frequency of drought occurrence. S_{R20y} , i.e.
 267 the root zone storage capacity required to overcome a drought once in 20 years, is used as the proxy for



268 S_{uMax} due to the assumption of a “cost” minimization strategy of plants as we mentioned above (Milly,
269 1994), and the fact that S_{R20y} has the best fit with S_{uMax} (Gao et al., 2014a).

270 Eventually, with the MCT approach to estimate S_{uMax} and the HSC curve to represent the root zone storage
271 capacity spatial distribution, the HSC-MCT runoff generation module is created, without free parameters.
272 It is worth noting that both the HSC-MCT and HSC modules are based on the HAND derived S_u - A_s relation,
273 and their distinction lays in the methods to obtain S_{uMax} . So far, the HBV power function module has 2 free
274 parameters (S_{uMax} , β). While the TOPMODEL and the HSC both have one free parameter (S_{uMax}). Ultimately
275 the HSC-MCT has no free parameter.

276 2.4 Interception, evaporation and routing modules

277 Except for the runoff generation module in the root zone reservoir (S_{UR}), we need to consider other
278 processes, including interception (S_{IR}) before the S_{UR} module, evaporation from the S_{UR} and the response
279 routine (S_{FR} and S_{SR}) after runoff generation from S_{UR} (Figure 4). Precipitation is firstly intercepted by
280 vegetation canopies. In this study, the interception was estimated by a threshold parameter (S_{IMax}), set to
281 2 mm (Gao et al., 2014a), below which all precipitation will be intercepted and evaporated (Equation 9)
282 (de Groen and Savenije, 2006). For the S_{UR} reservoir, we can either use the HBV beta-function (Equation
283 12), the runoff generation module of TOPMODEL (Equation 2-4) or the HSC module (Section 2.3) to
284 partition precipitation into generated runoff (R_u) and infiltration. The actual evaporation (E_a) from the soil
285 equals to the potential evaporation (E_p), if S_u/S_{uMax} is above a threshold (C_e), where S_u is the soil moisture
286 and S_{uMax} is the catchment averaged storage capacity. And E_a linearly reduces with S_u/S_{uMax} , while S_u/S_{uMax}
287 is below C_e (Equation 13). The E_p can be calculated by the Hargreaves equation (Hargreaves and Samani,
288 1985), with maximum and minimum daily temperature as input. The generated runoff (R_u) is further split
289 into two fluxes, including the flux to the fast response reservoir (R_f) and the flux to the slow response
290 reservoir (R_s), by a splitter (D) (Equation 14, 15). The delayed time from rainfall peak to the flood peak is
291 estimated by a convolution delay function, with a delay time of T_{lagF} . Subsequently, the fluxes into two
292 different response reservoirs (S_{FR} and S_{SR}) were released by two linear equations between discharge and
293 storage (Equation 19, 21), representing the fast response flow and the slow response flow mainly from
294 groundwater reservoir. The two discharges (Q_f and Q_s) generated the simulated streamflow (Q_m). The
295 model parameters are shown in Table 1, while the equations are given in Table 2. More detailed
296 description of the model structure can be referred to Gao et al., 2014b and 2016. It is worth underlining
297 that the only difference among the benchmark HBV type, TOPMODEL type, the HSC and the HSC-MCT



298 models is their runoff generation modules. Eventually, there are 7 free parameters in HBV model, 6 in
299 TOPMODEL and HSC model, and 5 in the HSC-MCT model.

300 2.5 Model evaluation, calibration, validation and models comparison

301 Two objective functions were used to evaluate model performance, since multi-objective evaluation is a
302 more robust approach to quantifying model performance with different criteria than a single one. The
303 Kling-Gupta efficiency (Gupta *et al.*, 2009) (I_{KGE}) was used as the criteria to evaluate model performance
304 and as an objective function for calibration. The equation is written as:

$$305 \quad I_{KGE} = 1 - \sqrt{(r-1)^2 + (\alpha-1)^2 + (\varepsilon-1)^2} \quad (7)$$

306 Where r is the linear correlation coefficient between simulation and observation; α ($\alpha = \sigma_m / \sigma_o$) is a
307 measure of relative variability in the simulated and observed values, where σ_m is the standard deviation
308 of simulated streamflow, and σ_o is the standard deviation of observed streamflow; ε is the ratio between
309 the average value of simulated and observed data. And the I_{KGL} (I_{KGE} of the logarithmic flows) (Fenicia *et al.*,
310 2007; Gao *et al.*, 2014b) is used to evaluate the model performance on baseflow simulation. Since the
311 response module, determined the baseflow simulation and I_{KGL} , is kept the same for all four models, thus
312 only the I_{KGE} results are presented in the results.

313 A multi-objective parameter optimization algorithm (MOSCEM-UA) (Vrugt *et al.*, 2003) was applied for
314 the calibration. The parameter sets on the Pareto-frontier of the multi-objective optimization were
315 assumed to be the behavioral parameter sets and can equally represent model performance. The
316 averaged hydrograph obtained by all the behavioral parameter sets were regarded as the simulated result
317 of that catchment for further studies. The number of complexes in MOSCEM-UA were set as the number
318 of parameters (7 for HBV, 6 for TOPMODEL and the HSC model, and 5 for HSC-MCT model), and the
319 number of initial samples was set to 210 and a total number of 50000 model iterations for all the
320 catchment runs. For each catchment, the first half period of data was used for calibration, and the other
321 half was used to do validation.

322 In module comparison, we defined three categories: if the difference of I_{KGE} of model A and model B in
323 validation is less than 0.1, model A and B are regarded as “equally well”. If the I_{KGE} of model A is larger
324 than model B in validation by 0.1 or more, model A is regarded as outperforming model B. If the I_{KGE} of
325 model A is less than model B in validation by -0.1 or less, model B is regarded to outperform model A.



326 3 Dataset

327 3.1 The Bruntland Burn catchment

328 The 3.2 km² Bruntland Burn catchment (Figure 5), located in north-eastern Scotland, was used as a
329 benchmark study to test the models performance based on a rich data base of hydrological measurements.
330 The Bruntland Burn is typical many upland catchments in North West Europe (e.g. Birkel et al., 2010),
331 namely a combination of steep and rolling hillslopes and over-widened valley bottoms due to the glacial
332 legacy of this region. The valley bottom areas are covered by deep (in parts > 30m) glacial drift deposits
333 (e.g. till) containing a large amount of stored water superimposed on a relatively impermeable granitic
334 solid geology (Soulsby et al., 2016). Peat soils developed (> 1m deep) in these valley bottom areas, which
335 remain saturated throughout most of the year with a dominant near-surface runoff generation
336 mechanism delivering runoff quickly via micro-topographical flow pathways connected to the stream
337 network (Soulsby et al., 2015). Brown rankers, peaty rankers and peat soils are responsible for a flashy
338 hydrological regime driven by saturation excess overland flow, while humus iron podzols on the hillslopes
339 do not favor near-surface saturation but rather facilitate groundwater recharge through vertical water
340 movement (Tetzlaff et al., 2014). Land-use is dominated by heather moorland, with smaller areas of rough
341 grazing and forestry on the lower hillslopes. Its annual precipitation is 1059 mm, with the summer months
342 (May-August) generally being the driest (Ali et al., 2013). Snow makes up less than 10% of annual
343 precipitation and melts rapidly below 500m. The evapotranspiration is around 400 mm per year and
344 annual discharge around 659 mm.

345 The LiDAR-derived DEM map with 2m resolution shows elevation ranging from 250m to 539m (Figure 5).
346 There are 7 saturation area maps (Figure 6) (May 2, July 2, August 4, September 3, October 1, November
347 26, in 2008, and January 21, in 2009), measured directly by field mapping (Ali et al., 2013), and a global
348 positioning system (GPS) was used to delineate the boundary of saturation areas. These saturation area
349 maps revealed a dynamic behavior of expanding and contracting areas connected to the stream network
350 that were used as a benchmark test for the HSC module.

351 3.2 MOPEX dataset

352 The MOPEX dataset was collected for a hydrological model parameter estimation experiment (Duan et al.,
353 2006; Schaake et al., 2006), containing 438 catchments in the CONUS (Contiguous United States). The
354 dataset contains the daily precipitation, daily maximum and minimum air temperature, and daily
355 streamflow. The longest time series range from 1948 to 2003. 323 catchments were used in this study,



356 with areas between 67 and 10,329 km², and excluding the catchments with data records <30 years,
357 impacted by snowmelt or with extreme arid climate (aridity index $E_p/P > 2$). The daily streamflow was used
358 to calibrate the free parameters, and validate the models. The Digital Elevation Model (DEM) of the
359 CONUS in 90m resolution was download from the Earth Explorer of United States Geological Survey (USGS,
360 <http://earthexplorer.usgs.gov/>).

361 4 Results of the Bruntland Burn

362 4.1 Topography analysis

363 The TWI map of the BB (Figure 5) was generated from its DEM. Overall, the TWI map, ranging from -0.4
364 to 23.4, mainly differentiates the valley bottom areas with the highest TWI values from the steeper slopes.
365 This is probably caused by the fine resolution of the DEM map in 2 m, since previous research found the
366 sensitivity of TWI to DEM resolution (Sørensen and Seibert, 2007). From the TWI map, the frequency
367 distribution function and the accumulative frequency distribution function can be derived (Figure 7), with
368 one unit of TWI as interval.

369 The generated HAND map, derived also from the DEM, is shown in Figure 5, with HAND values ranging
370 from 0m to 234m. Since HAND is sensitive to the definition of the perennial channel, which is highly
371 impacted by the stream initiation threshold area (Montgomery and Dietrich, 1989; Gharari et al., 2011;
372 Hooshyar et al., 2016). The start area was chosen as 40ha to maintain a close correspondence with
373 observed stream network. Based on the HAND map, we can derive the S_u-A_s curve (Figure 7) by analyzing
374 the HAND map with the method in Section 2.3.

375 4.2 Model performance

376 The observed and simulated hydrographs of three models (HBV, TOPMODEL, and HSC) in 2008 are shown
377 in Figure 8. We found all the three models can perform well to reproduce the observed hydrograph. The
378 k_{GE} of the three models are all around 0.66, which is largely in line with other studies from the BB (Birkel
379 et al, 2010; 2014). Since the measured rainfall-runoff time series only last from 2008 to 2014, which is too
380 short to estimate the S_{R20y} (proxy for $S_{U_{Max}}$) by MCT approach (which needs long-term hydro-
381 meteorological observation data,) the HSC-MCT model was not applied to the catchment.

382 The normalized relative soil moisture of the three model simulations are presented in Figure 8. Their
383 temporal fluctuation patterns are comparable. Nevertheless, the simulated soil moisture by TOPMODEL
384 has a larger variation, compared with HBV and HSC (Figure 8).



385 Figure 7 shows the calibrated power curve from HBV (beta=0.98) with the S_u-A_s curve obtained from the
386 HSC module. We found the two curves are largely comparable, especially while the relative soil moisture
387 is low. This result demonstrates that for the BB with glacial drift deposits and combined terrain of steep
388 and rolling hillslopes and over-widened valley bottoms, the HBV power curve can essentially be derived
389 from the S_u-A_s curve of HSC module merely by topographic information without calibration.

390 4.3 Contributing area simulation

391 The observed saturation area and the simulated contributing area from both TOPMODEL and the HSC are
392 shown in Figure 6, 8, 9. We found although both modules overestimated the contributing areas, they can
393 capture the temporal variation. For example, the smallest saturated area both observed and simulated
394 occurred on July-02-2008, and the largest saturated area both occurred on January-21-2009. Comparing
395 the estimated contributing area of TOPMODEL with the HSC module, we found the results of the HSC
396 correlates better ($R^2=0.60$) with the observed saturated areas than TOPMODEL ($R^2=0.50$) (Figure 9). For
397 spatial patterns, the results of the HSC module are also more closely comparable with the observed
398 saturated areas than TOPMODEL (Figure 6). Based on these results benchmarking the HSC module with
399 observed saturated area maps, we proceeded to test HSC for a wide range of climatically and
400 geomorphologically different catchments across the US.

401 5 Results from the MOPEX catchments

402 5.1 Topography analysis of the Contiguous US and 323 MOPEX catchments

403 To delineate the TWI map for the CONUS, the depressions of the DEM were firstly filled with a threshold
404 height of 100m (recommended by Esri). The slope map, i.e. the steepest local slope, was generated by the
405 filled DEM, and the flow direction map was also derived from the filled DEM using the D8 algorithm
406 (O'Callaghan and Mark, 1984; Jenson and Domingue, 1988). Subsequently, the flow accumulation map
407 could be generated from the flow direction map. The accumulated upslope area (A), obtained from the
408 flow accumulation map, was then divided by an estimate of the contour length (L), which is related to the
409 flow direction map, to provide the local upslope area draining through a certain point per unit contour
410 length ($a = A/L$). With the definition of TWI as $\ln(a/\tan \beta)$, the TWI map of the CONUS is produced (Figure
411 S1). From the TWI map of the CONUS, we clipped the TWI maps for the 323 MOPEX catchments with their
412 catchment boundaries. And then the TWI frequency distribution and the accumulated frequency
413 distribution of the 323 MOPEX catchments (Figure S2), with one unit of TWI as interval, were derived
414 based on the 323 TWI maps.



415 The HAND map (Figure 10) was also generated from the filled DEM, with the input of the flow direction
416 and flow accumulation maps. Specifically, the perennial river network was obtained, based on the flow
417 accumulation map, by setting the stream initiation area threshold of 500 grid cells (4.05 km²), which fills
418 in the range of stream initiation thresholds reported by others (e.g. Colombo et al., 2007; Moussa, 2008,
419 2009). In the end, HAND was then calculated from the elevation of each raster cell above nearest grid cell
420 flagged as stream cell following the flow direction (Gharari et al., 2011).

421 In Figure 10, it is shown that the regions with large HAND values are located in Rocky Mountains and
422 Appalachian Mountains, while the Great Plains has smaller HAND values. Interestingly, the Great Basin,
423 especially in the Salt Lake Desert, has small HAND values, illustrating its low elevation above the nearest
424 drainage, although their elevations above seas level are high. From the CONUS HAND map, we clipped the
425 HAND maps for the 323 MOPEX catchments with their catchment boundaries. We then plot their HAND-
426 area curves, following the procedures of II-IV in Section 2.2. Figure 11a shows the normalized HAND
427 profiles of the 323 catchments.

428 Based on the HAND profiles and the Step V in Section 2.2, we derived the normalized storage capacity
429 distribution for all catchments (Figure 11b). Subsequently, the root zone moisture and saturated area
430 relationship (A_s-S_u) can be plotted by the method in Step VI of Section 2.2. Lastly, reversing the curve of
431 A_s-S_u to S_u-A_s relation (Figure 11c), the latter one can be implemented to simulate runoff generation by
432 soil moisture. Figure 11c interestingly shows that in some catchments, there is almost no threshold
433 behavior between rainfall and runoff generation, where the catchments are covered by large areas with
434 low HAND values and limited storage capacity. Therefore, when rainfall occurs, wetlands response quickly
435 and generate runoff without a precipitation–discharge threshold relationship characteristic of areas with
436 higher moisture deficits. This is similar to the idea of FLEX-Topo where the storage capacity is distinguished
437 between wetlands and hillslopes, and on wetlands, with low storage capacity, where runoff response to
438 rainfall is almost instantaneous.

439 5.2 Model performance

440 Overall, the performance of the two benchmark models, i.e. HBV and TOPMODEL, for the MOPEX data
441 (Figure 12) is comparable with the previous model comparison experiments, conducted with four rainfall-
442 runoff models and four land surface parameterization schemes (Duan et al., 2006; Ye et al., 2014). The
443 median value of I_{KGE} of the HBV type model is 0.61 for calibration in the 323 catchments (Figure 12), and
444 averaged I_{KGE} in calibration is 0.62. In validation, the median and averaged values of I_{KGE} are kept the same
445 as calibration. The comparable performance of models in calibration and validation demonstrates the



446 robustness of benchmark models and the parameter optimization algorithm (i.e. MOSCEM-UA). The
447 TOPMODEL improves the median value of I_{KGE} from 0.61 (HBV) to 0.67 in calibration, and from 0.61 (HBV)
448 to 0.67 in validation. But the averaged values of I_{KGE} for TOPMODEL are slightly decreased from 0.62 (HBV)
449 to 0.61 in both calibration and validation. The HSC module, by involving the HAND topographic
450 information without calibrating the β parameter, improves the median value of I_{KGE} to 0.68 for calibration
451 and 0.67 for validation. The averaged values of I_{KGE} in both calibration and validation are also increased to
452 0.65, comparing with HBV (0.62) and TOPMODEL (0.61). Furthermore, Figure 12 demonstrates that,
453 comparing with the benchmark HBV and TOPMODEL, not only the median and averaged values were
454 improved by the HSC module, but also the 25th and 75th percentiles and the lower whisker end, all have
455 been dramatically improved. These results indicate the HSC module improved model performance to
456 reproduce hydrograph, and simultaneously maintaining model robustness and consistency.

457 Additionally, for the median I_{KGE} value, the HSC-MCT leads to an improvement from 0.61 (HBV) to 0.65 in
458 calibration, and from 0.61 (HBV) to 0.64 in validation, but not as well performed as TOPMODEL (0.67 for
459 calibration and validation). For the averaged I_{KGE} values, they were slightly reduced from 0.62 (HBV) and
460 0.61 (TOPMODEL) to 0.59 for calibration and validation. Although the HSC-MCT did not perform as well
461 as the HSC module, considering there is no free parameters to calibrate, the median I_{KGE} value of 0.64
462 (HBV is 0.61) and averaged I_{KGE} of 0.59 (TOPMODEL is 0.61) are quite acceptable. In addition, the 25th and
463 75th percentiles and the lower whisker end of the HSC-MCT model are all improved compared to the HBV
464 model. Moreover, the largely comparable results between the HSC and the HSC-MCT modules
465 demonstrate the feasibility of the MCT method to obtain the $S_{U_{Max}}$ parameter and the potential for HSC-
466 MCT to be implemented in prediction of ungauged basins (PUB, cf. Sivapalan et al., 2003; Blöschl et al.,
467 2013; Hrachowitz et al., 2013). Since the response routines determining the baseflow simulation of the
468 four models are exactly the same, the results of I_{KGL} as an indicator to evaluate baseflow are not presented.

469 Figure 13 shows the spatial comparisons of the HSC and HSC-MCT models with the two benchmark models.
470 We found that the HSC performs “equally well” as HBV (the difference of I_{KGE} in validation ranges -0.1 ~
471 0.1) in 88% catchments, and in the remaining 12% of the catchments the HSC outperforms HBV (the
472 improvement of I_{KGE} in validation is larger than 0.1). In not a single catchment did the calibrated HBV
473 outperform the HSC. From the spatial comparison, we found that the catchments, where the HSC model
474 performed better are mostly located in the Great Plains, with modest sloping (4.0 degree), while the other
475 catchments have average slope of 8.1 degree. Comparing the HSC model with TOPMODEL, we found in
476 91% of the catchments that the two models have approximately equal performance. In 8% of the



477 catchments, the HSC model outperformed TOPMODEL. Only in 1% of the catchments (two in Appalachian
478 Mountain and one in the Rocky Mountain in California), TOPMODEL performed better. From spatial
479 analysis, we found the HSC outperformed catchments have flat terrain (2.3 degree) with moderate
480 averaged HAND value (26m), while the TOPMODEL outperformed catchments have steep hillslope (19
481 degree) with large averaged HAND value (154m).

482 Without calibration of S_{uMax} , as expected, the performance of HSC-MCT module slightly deteriorates
483 (Figure 12). In comparison with HBV, the outperformance reduced from 12% (HSC) to 4% (HSC-MCT), the
484 approximately equal-well simulated catchments dropped from 88% to 79%, and the inferior performance
485 increased from 0% to 17%. Also, in comparison with TOPMODEL, the better performance dropped from
486 8% (HSC model) to 7% (HSC-MCT model), the approximately equal catchments reduced from 91% to 72%,
487 and the inferior performance increased from 1% to 21%. The inferiority of the HSC-MCT model is probably
488 caused by the uncertainty of the MCT method for different ecosystems which have different survival
489 strategies and use different return periods to bridge critical drought periods. By using ecosystem
490 dependent return periods, this problem could be reduced (Wang-Erlandsson et al., 2016).

491 To further explore the reason for the better performance of the HSC approach, we selected the 08171000
492 catchment in Texas (Figure 13), in which both the HSC module and the HSC-MCT module outperformed
493 the two benchmark modules to reproduce the observed hydrograph (Figure S3). The HBV model
494 dramatically underestimated the peak flows, with I_{KGE} as 0.54, while TOPMODEL significantly
495 overestimated the peak flows, with I_{KGE} as 0.30. The HSC-MCT model improved the I_{KGE} to 0.71, and the
496 HSC model further enhanced I_{KGE} to 0.74.

497 Since the modules of interception, evaporation and routing are identical for the four models, the runoff
498 generation modules are the key to understand the difference in model performance. Figure S4 shows the
499 HBV β curve and the S_u-A_s curve of the HSC model, as well the TWI frequency distribution. We found that
500 with a given S_u/S_{uMax} , the HBV β function generates less contributing area than the HSC model, which
501 explains the underestimation of the HBV model. In contrast, TOPMODEL has a sharp and steep
502 accumulated TWI frequency curve. In particular, the region with TWI=8 accounts for 40% of the catchment
503 area, and over 95% of the catchment areas are within the TWI ranging from 6 to 12. This indicates that
504 even with low soil moisture content (S_u/S_{uMax}), the contributing area by TOPMODEL is relatively large,
505 leading to the sharply increased peak flows for all rainfall events.



506 6 Discussion

507 6.1 Rainfall-runoff processes and topography

508 In hillslope and catchment hydrology, the partitioning of precipitation into runoff and evaporation is a
509 fundamental function in virtually all hydrological models. Bucket-type models (e.g. HBV and Xinanjiang),
510 as one of the most widely used group of conceptual models, typically adopt two parameters to determine
511 runoff generation. One is the root zone storage capacity (S_{uMax}) and the other is the shape parameter (i.e.
512 β) determining the relation between root zone moisture and runoff generation. In long-term water
513 balance studies, climate plays a key role in determining the storage capacity and the partition between
514 evaporation and runoff (Budyko, 1971; Wang and Tang, 2014; Gao et al., 2014a). But for specific events,
515 the key question is how antecedent soil moisture impacts runoff generation. Field studies support that in
516 many mildly sloping catchments, SEF is the dominant runoff generation mechanism (Sklash and Farvolden,
517 1979; Burt and McDonnell, 2015). Therefore, it is essential to determine the temporal variability of the
518 saturated area (equal to the contributing area and the runoff coefficient of a specific rainfall-runoff event),
519 to calculate runoff generation. Linking the runoff contributing area to topography is not a new insight in
520 rainfall-runoff modelling. TOPMODEL is an elegant pioneering model allowing us to understand the
521 interaction between topography and connectivity. In this study, the HSC module uses a relatively new
522 topographic index (i.e. HAND) to identify hydrological similarity.

523 We applied a novel approach to derive the relationship between soil moisture storage and the saturated
524 area from HAND. The areas with relatively low HAND values are saturated earlier than areas with higher
525 HAND values, due to the larger storage capacity in high HAND locations. The outperformance of the HSC
526 model over the benchmark HBV and TOPMODEL in modestly sloping catchments indicates that the HSC
527 module has a higher realism than the calibrated beta-function of the HBV model and the TWI of
528 TOPMODEL in these regions. Very interestingly, Fan et al., (2017) presented a global synthesis of 2,200
529 root observations of >1000 species, and revealed the systematic variation of rooting depth along HAND
530 (Fig.1, in Fan et al., 2017). Since rooting depth can be translated to root zone storage capacity through
531 combination with soil plant-available water (Wang-Erlandsson et al., 2016). This large sample dataset,
532 from ecological perspective, provides a strong support for the assumption of the HSC model on modest
533 slopes, i.e. the increase of root zone storage capacity with HAND. More interestingly, on excessively
534 drained uplands, rooting depth does not follow the same role, with shallow depth and limited to rain
535 infiltration (Fig.1, in Fan et al., 2017). This could explain the inferior performance of HSC model to
536 TOPMODEL in three MOPEX catchments (averaged HAND is 154 m) with excessively drained uplands,



537 where Hortonian overland flow is likely the dominant mechanism, and the HSC assumption likely does not
538 work well.

539 The FLEX-Topo model (Savenije, 2010) also uses HAND information as a topographic index to distinguish
540 between landscape-related runoff processes, and has both similarity and differences with the HSC model.
541 The results of the HSC model illustrate that the riparian areas are more prone to be saturated, which is
542 consistent with the concept of the FLEX-Topo model. Another important similarity of the two models is
543 their parallel model structure. From our perspective, the parallel model structure is closer to reality. Since
544 before saturation, rainfall is firstly infiltrated into local storage, and water moves vertically; only after a
545 certain level of saturation, water starts to move laterally. But in both models it is assumed that the upslope
546 area has larger storage capacity, therefore the upper land generates runoff later than the lower land. In
547 other words, in most cases, the local storage is saturated due to the local rainfall, instead of flow from
548 upslope. Therefore, the local storage is an essential feature, to estimate the saturated area and runoff
549 generation, rather than the water coming from uphill.

550 The most obvious difference between the HSC and the FLEX-Topo models is the approach towards
551 discretization of a catchment. The FLEX-Topo model classifies a catchment into various landscapes, e.g.
552 wetlands, hillslopes and plateau. This discretization method requires threshold values to classify
553 landscapes, i.e. threshold values of HAND and slope, which leads to fixed and time-independent
554 proportions of landscapes. The HSC model does not require landscape classification, which reduced the
555 subjectivity in discretization and restricted the model complexity, as well as simultaneously allowing the
556 fluctuation of saturated areas (termed as wetlands in FLEX-Topo).

557 6.2 Catchment heterogeneity and simple models

558 Catchments exhibit a wide array of heterogeneity and complexity with spatial and temporal variations of
559 landscape characteristics and climate inputs. For example, the Darcy-Richards equation approach is often
560 consistent with point-scale measurements of matrix flow, but not for preferential flow caused by roots,
561 soil fauna and even cracks and fissures (Beven and Germann, 1982; Zehe and Fluehler, 2001; Weiler and
562 McDonnell, 2007). As a result, field experimentalists continue to characterize and catalogue a variety of
563 runoff processes, and hydrological and land surface modelers are developing more and more complicated
564 models to involve the increasingly detailed processes (McDonnell et al., 2007). However, there is still no
565 compelling evidence to support the outperformance of sophisticated “physically-based” models in terms
566 of higher equifinality and uncertainty than the simple lumped or semi-distributed conceptual models in
567 rainfall-runoff simulation (Beven, 1989; Orth et al., 2015).



568 But evidence is mounting that a catchment is not a random assemblage of different heterogeneous parts
569 (Sivapalan, 2009; Troch et al., 2013; Zehe et al., 2013), and conceptualising heterogeneities does not
570 require complex laws (Chase, 1992; Passalacqua et al., 2015). Asking questions of “why” rather than “what”
571 likely leads to more useful insights and a new way forward (McDonnell et al., 2007). Catchment is a
572 geomorphological and even an ecological system whose parts are related to each other probably due to
573 catchment self-organization and evolution (Sivapalan and Blöschl, 2015; Savenije and Hrachowitz, 2017).
574 This encourages the hope that simplified concepts may be found adequate to describe and model the
575 operation of the basin runoff generation process. It is clear that topography, with fractal characteristic
576 (Rodriguez-Iturbe and Rinaldo, 1997), is often the dominant driver of runoff, as well as being a good
577 integrated indicator for vegetation cover (Gao et al., 2014b), rooting depth (Fan et al., 2017), root zone
578 evaporation and transpiration deficits (Maxwell and Condon, 2016), soil properties (Seibert et al., 2007),
579 and even geology (Rempe and Dietrich, 2014; Gomes, 2016). Therefore, we argue that increasingly
580 detailed topographic information is an excellent integrated indicator allowing modelers to continue
581 systematically represent heterogeneities and simultaneously reduce model complexity. The model
582 structure and parametrization of both HSC and TOPMODEL are simple, but not over simplified, as they
583 capture probably the most dominant factor controlling runoff generation, i.e. the spatial heterogeneity of
584 storage capacity. Hence, this study also sheds light on the possibility of moving beyond heterogeneity and
585 process complexity (McDonnell et al., 2007), to simplify them into a succinct and *a priori* curve by taking
586 advantage of catchment self-organization probably caused by co-evolution or the principle of maximum
587 entropy production (Kleidon and Lorenz, 2004).

588 6.3 Implications and limitation

589 The calibration-free HSC-MCT runoff generation model may enhance our ability to predict runoff in
590 ungauged basins (Sivapalan et al., 2003; Blöschl et al., 2013; Hrachowitz et al., 2013). Hydrological models
591 still depend largely on observational data to feed statistical analysis and calibrate the free parameters.
592 This is probably not a major issue in the developed world, with abundant of comprehensive
593 measurements in many places, but for the developing world it requires prediction with sparse data and
594 fragmentary knowledge. Topographic information with high spatial resolution is freely available globally,
595 allowing us to implement the HSC model in global scale studies. In addition, thanks to the recent
596 development, testing, and validation of remote sensing evaporation products in large spatial scale (e.g.
597 Anderson et al., 2011; Hu and Jia, 2015), the S_{uMax} estimation has become possible without in situ hydro-



598 meteorological measurements (Wang-Erlandsson et al., 2016). These widely-accessible datasets make the
599 global-scale implementation of HSC-MCT module promising.

600 Finally, we should not ignore the limitations of this model, although it has better performance and
601 modelling consistency. Firstly, the threshold area for the initiating a stream was set as a constant value
602 for the entire CONUS, but the variation of this value in different climate, geology and landscape classes
603 (Montgomery and Dietrich, 1989; Helmlinger et al., 1993; Colombo et al., 2007; Moussa, 2008) needs to
604 be future investigated. Secondly, the discrepancy between observed and simulated saturation area needs
605 to be further investigated, by utilizing more advanced field measurement and simultaneously refining the
606 model assumption. The overestimation of the HSC model is possibly because two runoff generation
607 mechanisms – SOF and the SSF occur at the same time. However, the saturated area observed by the
608 “squishy boot” method (Ali et al., 2013), probably only distinguished the areas where SOF occurred.
609 Subsurface stormflow, also contributes to runoff but without surface runoff, cannot be observed by the
610 “squishy boot” method. Thus, this mismatch between simulation and observation probably leads to this
611 saturated area overestimation. Another interpretation might be the different definition of “saturation”.
612 The observed saturated areas are places where 100% of soil pore volume is filled by water. But the
613 modelled saturation areas are located where soil moisture is above field capacity, and not necessarily 100%
614 filled with water, which probably also results in overestimation of saturated areas.

615 7 Summary and conclusions

616 In this study, we developed a simple, calibration-free hydrological module based on HAND information,
617 which is an excellent indicator of hydrologic similarity and a physically-based index linking terrain with
618 hydraulic gradient at the hillslope and catchment scales. We assumed that the local storage capacity is
619 closely linked to HAND. Based on this assumption and the HAND spatial distribution pattern, the soil
620 moisture (S_u) - saturated area (A_s) relation for each catchment was derived, which was used to estimate
621 the A_s of specific rainfall event based on continuous calculation of S_u . Subsequently, based on the S_u - A_s
622 relation, the HAND-based Storage Capacity curve (HSC) module was developed. Then, applying the mass
623 curve technique (MCT) approach (Gao et al., 2014a), we estimated the root zone storage capacity (S_{uMax})
624 from observed hydro-climatological and vegetation data, and coupled it with HSC to create the
625 calibration-free HSC-MCT module, in which the S_{uMax} was obtained by MCT, and the S_u - A_s relation was
626 obtained by HSC. The HBV beta-function and TWI-based TOPMODEL were used as two benchmark
627 modules to test the performance of HSC and HSC-MCT on both hydrograph simulation and ability to
628 reproduce the contributing area, which was measured for different hydrometeorological conditions in the



629 Bruntland Burn catchment in Scotland. Subsequently, 323 MOPEX catchments in the US were used as a
630 large sample hydrological study to further validate the effectiveness of our proposed runoff generation
631 modules.

632 In the BB exploratory study, we found that the HSC, HBV and TOPMODEL performed comparably well to
633 reproduce the observed hydrograph. Interestingly, the S_u-A_s curves of HSC and HBV are largely comparable,
634 which illustrates the HSC curve can be used as a proxy for the HBV beta-function. Comparing the estimated
635 contributing area of TOPMODEL with the HSC module, we found that the results of the HSC module
636 correlate better ($R^2=0.60$) with the observed saturated areas compared to TOPMODEL ($R^2=0.50$). This
637 likely indicates that HAND maybe a better indicator to distinguish hydrological similarity than TWI.

638 For the 323 MOPEX catchments, HSC improved the averaged validation value of I_{KGE} from 0.62 (HBV) and
639 0.61 (TOPMODEL) to 0.65. In 12% of the MOPEX catchments, the HSC module outperforms HBV, and in
640 not a single catchment did the calibrated HBV outperform the HSC. Comparing with TOPMODEL, the HSC
641 outperformed in 8% of the catchments, and in only 1% of catchments TOPMODEL has a better
642 performance. Not surprisingly, the I_{KGE} of HSC-MCT model was slightly reduced to 0.59, due to the non-
643 calibrated S_{uMax} , but still comparably well performed as HBV (0.62) and TOPMODEL (0.61). This illustrates
644 the robustness of both the HSC approach to derive the spatial distribution of the root zone storage
645 capacity (β) and the efficiency of the MCT method to estimate the root zone storage capacity (S_{uMax}).
646 Moreover, the new module allows us to map out the saturated area, which has potential capability to be
647 used for broader hydrological, ecological, climatological, geomorphological, and biogeochemical studies.

648

649 **Acknowledgement:**

650 This study was supported by National Key R&D Program of China (2017YFE0100700).

651

652 **Author contributions:**

653 H.G. and H.H.G.S. designed research; H.G. performed research; C.B., C.S., D.T and H.G. provided data,
654 among which the dynamics of the saturation areas data in the BB was provided by C.B. C.S., and D.T.; H.G.
655 analysed data; C.B. was involved in the interpretation of some of the modelling work in the BB; H.G. M.H,
656 and H.H.G.S. wrote the paper; CS and DT extensively edited the paper, and provided substantial comments
657 and constructive suggestions for scientific clarification.



658

659 References:

- 660 Anderson, M. C., Kustas, W. P., Norman, J. M., Hain, C. R., Mecikalski, J. R., Schultz, L., González-Dugo, M.
661 P., Cammalleri, C., D'Urso, G., Pimstein, A., and Gao, F.: Mapping daily evapotranspiration at field to
662 continental scales using geostationary and polar orbiting satellite imagery, *Hydrol. Earth Syst. Sci.*, 15,
663 223–239, doi:10.5194/hess-15-223-2011, 2011.
- 664 Andréassian V, Bourgin F, Oudin L, Mathevet T, Perrin C, Lerat J, Coron L, Berthet L. 2014. Seeking
665 genericity in the selection of parameter sets: Impact on hydrological model efficiency. *Water Resources*
666 *Research* 50 (10): 8356–8366
- 667 Bergström S, Forsman A. 1973. Development of a conceptual deterministic rainfall-runoff model.
668 *Hydrology Research* 4 (3): 147–170
- 669 Bergström S, Lindström G. 2015. Interpretation of runoff processes in hydrological modelling—experience
670 from the HBV approach. *Hydrological Processes* 29 (16): 3535–3545
- 671 Beven K. 2004. Robert E. Horton's perceptual model of infiltration processes. *Hydrological Processes* 18
672 (17): 3447–3460 DOI: 10.1002/hyp.5740
- 673 Beven K, Freer J. 2001. A dynamic TOPMODEL. *Hydrological Processes* 15 (10): 1993–2011 DOI:
674 10.1002/hyp
- 675 Beven K. 1993. Prophecy, reality and uncertainty in distributed hydrological modelling. *Advances in Water*
676 *Resources* 16 (1): 41–51 DOI: [http://dx.doi.org/10.1016/0309-1708\(93\)90028-E](http://dx.doi.org/10.1016/0309-1708(93)90028-E)
- 677 Beven K. 1995. Linking parameters across scales: Subgrid parameterizations and scale dependent
678 hydrological models. *Hydrological Processes* 9 (September 1994): 507–525 DOI:
679 10.1002/hyp.3360090504.252
- 680 Beven KJ. 2012. *Rainfall–Runoff Models: The Primer*
- 681 Beven K., Germann P. 1982. Macropores and water-flow in soils. *Water Resour. Res.* 18, 1311–1325
- 682 Beven KJ, Kirkby MJ. 1979. A physically based, variable contributing area model of basin hydrology.
683 *Hydrological Sciences Bulletin* 24 (1): 43–69 DOI: 10.1080/02626667909491834
- 684 Beven, K., 1989. Changing ideas in hydrology – the case of physically-based models. *J. Hydrol.* 105 (1–2),
685 157–172.



- 686 Birkel C, Tetzlaff D, Dunn SM, Soulsby C. 2010. Towards a simple dynamic process conceptualization in
687 rainfall–runoff models using multi-criteria calibration and tracers in temperate, upland catchments.
688 *Hydrological Processes* 24 (3): 260–275
- 689 Birkel, C., Soulsby, C., and D. Tetzlaff (2014) Conceptual modelling to assess how the interplay of
690 hydrological connectivity, catchment storage and tracer dynamics controls non-stationary water age
691 estimates. *Hydrological Processes*, DOI: 10.1002/hyp.10414.
- 692 Blöschl G. 2013. *Runoff prediction in ungauged basins: synthesis across processes, places and scales.*
693 Cambridge University Press.
- 694 Budyko MI. 1971. *Climate and life*
- 695 Burt TP, McDonnell JJ. 2015. Whither field hydrology? The need for discovery science and outrageous
696 hydrological hypotheses. *Water Resources Research* 51 (8): 5919–5928 DOI: 10.1002/2014WR016839
- 697 Chase CG. 1992. Fluvial landsculpting and the fractal dimension of topography. *Geomorphology* 5 (1): 39–
698 57 DOI: [http://dx.doi.org/10.1016/0169-555X\(92\)90057-U](http://dx.doi.org/10.1016/0169-555X(92)90057-U)
- 699 Clark MP, Slater AG, Rupp DE, Woods R a., Vrugt J a., Gupta H V., Wagener T, Hay LE. 2008. Framework
700 for Understanding Structural Errors (FUSE): A modular framework to diagnose differences between
701 hydrological models. *Water Resources Research* 44: 1–14 DOI: 10.1029/2007WR006735
- 702 Clark, Martyn P., Dmitri Kavetski, and Fabrizio Fenicia. “Pursuing the Method of Multiple Working
703 Hypotheses for Hydrological Modeling.” *Water Resources Research* 47.9 (2011): 1–16.
- 704 Colombo R, Vogt J V, Soille P, Paracchini ML, de Jager A. 2007. Deriving river networks and catchments at
705 the European scale from medium resolution digital elevation data. *CATENA* 70 (3): 296–305 DOI:
706 <http://doi.org/10.1016/j.catena.2006.10.001>
- 707 Condon, Laura E, and Reed M Maxwell. “Evaluating the Relationship between Topography and
708 Groundwater Using Outputs from a Continental-Scale Integrated Hydrology Model.” *Water Resources*
709 *Research* 51.8 (2015): 6602–6621.
- 710 Duan Q, Schaake J, Andréassian V, Franks S, Goteti G, Gupta HV, Gusev YM, Habets F, Hall a., Hay L, et al.
711 2006. Model Parameter Estimation Experiment (MOPEX): An overview of science strategy and major
712 results from the second and third workshops. *Journal of Hydrology* 320 (1-2): 3–17 DOI:
713 10.1016/j.jhydrol.2005.07.031



- 714 Dunne T, Black RD. 1970. to Storm Runo in a Small NeW , England Watershed Dense , till. Water Resources
715 Research 6 (5): 1296–1311 Available at:
716 <http://soilandwater.bee.cornell.edu/Research/VSA/papers/DunneWRR70.pdf>
- 717 Boer-Euser, T. ., H. K. McMillan, M. Hrachowitz, H. C. Winsemius, and H. H. G. Savenije (2016), Influence
718 of soil and climate on root zone storage capacity, Water Resour. Res., 52, 2009–2024,
719 doi:10.1002/2015WR018115.
- 720 Fan, Y., Miguezmacho, G., Jobbágy, E. G., Jackson, R. B., & Oterocasal, C. (2017). Hydrologic regulation of
721 plant rooting depth. Proceedings of the National Academy of Sciences of the United States of America,
722 114(40), 201712381.
- 723 Fenicia F, Savenije HHG, Matgen P, Pfister L. 2007. A comparison of alternative multiobjective calibration
724 strategies for hydrological modeling. Water Resources Research 43 (3): n/a–n/a DOI:
725 10.1029/2006WR005098
- 726 Gao H, Hrachowitz M, Schymanski SJ, Fenicia F, Sriwongsitanon N, Savenije HHG. 2014a. Climate controls
727 how ecosystems size the root zone storage capacity at catchment scale. Geophysical Research Letters 41
728 (22): 7916–7923 DOI: 10.1002/2014gl061668
- 729 Gao H, Hrachowitz M, Fenicia F, Gharari S, Savenije HHG. 2014b. Testing the realism of a topography-
730 driven model (FLEX-Topo) in the nested catchments of the Upper Heihe, China. Hydrology and Earth
731 System Sciences 18 (5): 1895–1915 DOI: 10.5194/hess-18-1895-2014
- 732 Gao H, Hrachowitz M, Sriwongsitanon N, Fenicia F, Gharari S, Savenije HHG. 2016. Accounting for the
733 influence of vegetation and landscape improves model transferability in a tropical savannah region. Water
734 Resources Research 52 (10): 7999–8022 DOI: 10.1002/2016WR019574
- 735 Gao H, Cai H, Zheng D. 2017. Understand the impacts of landscape features on the shape of storage
736 capacity curve and its influence on flood. Hydrology Research. DOI: Hydrology-D-16-00245R3
- 737 Gao J, Holden J, Kirkby M. 2016. The impact of land-cover change on flood peaks in peatland basins. Water
738 Resources Research 52 (5): 3477–3492 DOI: 10.1002/2015WR017667
- 739 Gharari S, Hrachowitz M, Fenicia F, Savenije HHG. 2011. Hydrological landscape classification:
740 investigating the performance of HAND based landscape classifications in a central European meso-scale
741 catchment. Hydrology and Earth System Sciences 15 (11): 3275–3291 DOI: 10.5194/hess-15-3275-2011



- 742 Gharari S, Hrachowitz M, Fenicia F, Gao H, Savenije HHG. 2014. Using expert knowledge to increase
743 realism in environmental system models can dramatically reduce the need for calibration. *Hydrology and*
744 *Earth System Sciences* 18 (12): 4839–4859 DOI: 10.5194/hess-18-4839-2014
- 745 Gharari, S. On the role of model structure in hydrological modeling: Understanding models, PhD
746 dissertation, 2016
- 747 Gomes GJC, Vrugt JA, Vargas EA. 2016. Toward improved prediction of the bedrock depth underneath
748 hillslopes: Bayesian inference of the bottom-up control hypothesis using high-resolution topographic data.
749 *Water Resources Research* 52 (4): 3085–3112 DOI: 10.1002/2015WR018147
- 750 Grabs T, Seibert J, Bishop K, Laudon H. 2009. Modeling spatial patterns of saturated areas: A comparison
751 of the topographic wetness index and a dynamic distributed model. *Journal of Hydrology* 373 (1): 15–23
- 752 De Groen MM, Savenije HHG. 2006. A monthly interception equation based on the statistical
753 characteristics of daily rainfall. *Water Resources Research* 42 (12): n/a–n/a DOI: 10.1029/2006WR005013
- 754 Gumbel, E. J. (1935), Les valeurs extrêmes des distributions statistiques, *Annales de l’institut Henri*
755 *Poincaré*, 5(2), 115–158.
- 756 Gupta H V., Kling H, Yilmaz KK, Martinez GF. 2009. Decomposition of the mean squared error and NSE
757 performance criteria: Implications for improving hydrological modelling. *Journal of Hydrology* 377 (1-2):
758 80–91 DOI: 10.1016/j.jhydrol.2009.08.003
- 759 Hargreaves GH, Samani ZA. 1985. Reference crop evapotranspiration from temperature. *Applied*
760 *engineering in agriculture* 1 (2): 96–99
- 761 Haria AH, Shand P. 2004. Evidence for deep sub-surface flow routing in forested upland Wales:
762 implications for contaminant transport and stream flow generation. *Hydrology and Earth System Sciences*
763 *Discussions* 8 (3): 334–344
- 764 Harte J. 2002. Toward a synthesis of the Newtonian and Darwinian worldviews. *Physics Today* 55 (10): 29–
765 34 DOI: 10.1063/1.1522164
- 766 Helmlinger KR, Kumar P, Foufoula-Georgiou E. 1993. On the use of digital elevation model data for
767 Hortonian and fractal analyses of channel network. *Water Resources Research* 29: 2599–2613.
- 768 Hewlett JD. 1961. Soil moisture as a source of base flow from steep mountain watersheds. Southeastern
769 Forest Experiment Station, US Department of Agriculture, Forest Service.



- 770 Hewlett JD, Troendle CA. 1975. Non point and diffused water sources: a variable source area problem. In
771 Watershed Management; Proceedings of a Symposium.
- 772 Hooshyar M, Wang D, Kim S, Medeiros SC, Hagen SC. 2016. Valley and channel networks extraction based
773 on local topographic curvature and k-means clustering of contours. *Water Resources Research* 52 (10):
774 8081–8102
- 775 Horton, R.E., 1933. The role of infiltration in the hydrologic cycle. *Trans. Am. Geophys. Union* 14, 446–460.
- 776 Hrachowitz M, Savenije HHG, Blöschl G, McDonnell JJ, Sivapalan M, Pomeroy JW, Arheimer B, Blume T,
777 Clark MP, Ehret U, et al. 2013. A decade of Predictions in Ungauged Basins (PUB)—a review. *Hydrological
778 Sciences Journal* 58 (6): 1198–1255 DOI: 10.1080/02626667.2013.803183
- 779 Hu, G. and Jia, L.: Monitoring of evapotranspiration in a semiarid inland river basin by combining
780 microwave and optical remote sensing observations, *Remote Sens.*, 7, 3056–3087,
781 doi:10.3390/rs70303056, 2015.
- 782 Iorgulescu I, Jordan J-P. 1994. Validation of TOPMODEL on a small Swiss catchment. *Journal of Hydrology*
783 159 (1): 255–273 DOI: [http://dx.doi.org/10.1016/0022-1694\(94\)90260-7](http://dx.doi.org/10.1016/0022-1694(94)90260-7)
- 784 Jenson SK, Domingue JO. 1988. Extracting topographic structure from digital elevation data for geographic
785 information system analysis. *Photogrammetric engineering and remote sensing* 54 (11): 1593–1600
- 786 Kirchner JW. 2006. Getting the right answers for the right reasons: Linking measurements, analyses, and
787 models to advance the science of hydrology. *Water Resources Research* 42 (3): n/a–n/a DOI:
788 10.1029/2005WR004362
- 789 Kleidon A, Lorenz RD. 2004. *Non-equilibrium thermodynamics and the production of entropy: life, earth,
790 and beyond.* Springer Science & Business Media.
- 791 Liang X, Lettenmaier DP, Wood EF, Burges SJ. 1994. A simple hydrologically based model of land surface
792 water and energy fluxes for general circulation models. *Journal of Geophysical Research* 99 (D7): 14415
793 DOI: 10.1029/94JD00483
- 794 Liu D, Tian F, Hu H, Hu H. 2012. The role of run-on for overland flow and the characteristics of runoff
795 generation in the Loess Plateau, China. *Hydrological Sciences Journal* 57 (6): 1107–1117 DOI:
796 10.1080/02626667.2012.695870



- 797 Maxwell, Reed M, and Laura E Condon. "Connections between Groundwater Flow and Transpiration
798 Partitioning." *Science* 353.6297 (2016): 377 LP – 380.
- 799 McDonnell JJ, Sivapalan M, Vaché K, Dunn S, Grant G, Haggerty R, Hinz C, Hooper R, Kirchner J, Roderick
800 ML, et al. 2007. Moving beyond heterogeneity and process complexity: A new vision for watershed
801 hydrology. *Water Resources Research* 43 (7): n/a–n/a DOI: 10.1029/2006WR005467
- 802 McDonnell JJ. 2013. Are all runoff processes the same? *Hydrological Processes* 27 (26): 4103–4111 DOI:
803 10.1002/hyp.10076
- 804 Merz R, Blöschl G. 2004. Regionalisation of catchment model parameters. *Journal of Hydrology* 287 (1-4):
805 95–123 DOI: 10.1016/j.jhydrol.2003.09.028
- 806 Milly, P. C. D. (1994), Climate, soil water storage, and the average annual water balance, *Water Resour.*
807 *Res.*, 30(7), 2143–2156.
- 808 Molenat J, Gascuel-Oudou C, Ruiz L, Gruau G. 2008. Role of water table dynamics on stream nitrate export
809 and concentration in agricultural headwater catchment (France). *Journal of Hydrology* 348 (3): 363–378
- 810 Molénat J, Gascuel-Odou C, Davy P, Durand P. 2005. How to model shallow water-table depth variations:
811 the case of the Kervidy-Naizin catchment, France. *Hydrological Processes* 19 (4): 901–920
- 812 Montgomery DR, Dietrich WE. 1989. Source areas, drainage density, and channel initiation. *Water*
813 *Resources Research* 25 (8): 1907–1918
- 814 Moussa R. 2008. Effect of channel network topology, basin segmentation and rainfall spatial distribution
815 on the geomorphologic instantaneous unit hydrograph transfer function. *Hydrological Processes* 22 (3):
816 395–419 DOI: 10.1002/hyp.6612
- 817 Moussa R. 2009. Definition of new equivalent indices of Horton-Strahler ratios for the derivation of the
818 Geomorphological Instantaneous Unit Hydrograph. *Water Resources Research* 45 (9): n/a–n/a DOI:
819 10.1029/2008WR007330
- 820 Neuweiler I, Helmig R. Debates—Hypothesis testing in hydrology: A subsurface perspective. *Water*
821 *Resources Research*: n/a–n/a DOI: 10.1002/2016WR020047
- 822 Nobre a. D, Cuartas L a., Hodnett M, Rennó CD, Rodrigues G, Silveira a., Waterloo M, Saleska S. 2011.
823 Height Above the Nearest Drainage - a hydrologically relevant new terrain model. *Journal of Hydrology*
824 404 (1-2): 13–29 DOI: 10.1016/j.jhydrol.2011.03.051



- 825 O'Callaghan JF, Mark DM. 1984. The extraction of drainage networks from digital elevation data.
826 Computer vision, graphics, and image processing 28 (3): 323–344
- 827 Orth R, Staudinger M, Seneviratne SI, Seibert J, Zappa M. 2015. Does model performance improve with
828 complexity? A case study with three hydrological models. Journal of Hydrology 523: 147–159 DOI:
829 <http://doi.org/10.1016/j.jhydrol.2015.01.044>
- 830 Passalacqua P, Belmont P, Staley DM, Simley JD, Arrowsmith JR, Bode CA, Crosby C, DeLong SB, Glenn NF,
831 Kelly SA, et al. 2015. Analyzing high resolution topography for advancing the understanding of mass and
832 energy transfer through landscapes: A review. Earth-Science Reviews 148: 174–193 DOI:
833 <http://doi.org/10.1016/j.earscirev.2015.05.012>
- 834 Pelletier JD, Barron-Gafford GA, Breshears DD, Brooks PD, Chorover J, Durcik M, Harman CJ, Huxman TE,
835 Lohse KA, Lybrand R, et al. 2013. Coevolution of nonlinear trends in vegetation, soils, and topography with
836 elevation and slope aspect: A case study in the sky islands of southern Arizona. Journal of Geophysical
837 Research: Earth Surface 118 (2): 741–758 DOI: 10.1002/jgrf.20046
- 838 Perrin C, Michel C, Andréassian V. 2001. Does a large number of parameters enhance model performance?
839 Comparative assessment of common catchment model structures on 429 catchments. Journal of
840 Hydrology 242 (3-4): 275–301 DOI: 10.1016/S0022-1694(00)00393-0
- 841 Ponce, V. M., and R. H. Hawkins (1996), Runoff curve number: Has it reached maturity?, J. Hydrol. Eng.,
842 1(1), 11–19.
- 843 Rempe, D. M., and W. E. Dietrich (2014), A bottom-up control on fresh-bedrock topography under
844 landscapes, Proc. Natl. Acad. Sci. U. S. A., 111(18), 6576–6581, doi:10.1073/pnas.1404763111.
- 845 Rennó, C.D., Nobre, A.D., Cuartas, L.A., Soares, J.V., Hodnett, M.G., Tomasella, J., Waterloo, M., 2008.
846 HAND, a new terrain descriptor using SRTM-DEM; mapping terra-firme rainforest environments in
847 Amazonia. Remote Sensing of Environment 112, 3469–3481.
- 848 Rodriguez-Iturbe, I., and A. Rinaldo, Fractal River Basins: Chance and Self-Organization, Cambridge Univ.
849 Press, 547 pp., New York, 1997.
- 850 Samaniego L, Kumar R, Attinger S. 2010. Multiscale parameter regionalization of a grid-based hydrologic
851 model at the mesoscale. Water Resources Research 46 (5): n/a–n/a DOI: 10.1029/2008WR007327



- 852 Savenije HHG. 2009. HESS Opinions ‘The art of hydrology’. *Hydrology and Earth System Sciences* 13 (2):
853 157–161 DOI: 10.5194/hess-13-157-2009
- 854 Savenije, H. H. G.: HESS Opinions “Topography driven conceptual modelling (FLEX-Topo)”, *Hydrol. Earth*
855 *Syst. Sci.*, 14, 2681–2692, doi:10.5194/hess-14-2681-2010, 2010.
- 856 Savenije HHG, Hrachowitz M. 2017. HESS Opinions ‘Catchments as meta-organisms – a new blueprint for
857 hydrological modelling’. *Hydrol. Earth Syst. Sci.* 21 (2): 1107–1116 DOI: 10.5194/hess-21-1107-2017
- 858 Schaake, J., S. Cong, and Q. Duan (2006), The US MOPEX data set, *IAHS Publ.*, 307, 9.
- 859 Seibert J, Stendahl J, Sørensen R. 2007. Topographical influences on soil properties in boreal forests.
860 *Geoderma* 141 (1-2): 139–148 DOI: 10.1016/j.geoderma.2007.05.013
- 861 Shand P, Haria AH, Neal C, Griffiths K, Goody D, Dixon AJ, Hill T, Buckley DK, Cunningham J. 2005.
862 Hydrochemical heterogeneity in an upland catchment: further characterisation of the spatial, temporal
863 and depth variations in soils, streams and groundwaters of the Plynlimon forested catchment, Wales.
864 *Hydrology and Earth System Sciences* 9 (6): 621–644
- 865 Sørensen R, Seibert J. 2007. Effects of DEM resolution on the calculation of topographical indices: TWI and
866 its components. *Journal of Hydrology* 347 (1): 79–89 DOI:
867 <http://dx.doi.org/10.1016/j.jhydrol.2007.09.001>
- 868 Sivapalan M, Woods RA, Kalma JD. 1997. Variable bucket representation of TOPMODEL and investigation
869 of the effects of rainfall heterogeneity. *Hydrological processes* 11 (9): 1307–1330
- 870 Sivapalan M, Takeuchi K, Franks SW, Gupta VK, Karambiri H, Lakshmi V, Liang X, McDonnell JJ, Mendiondo
871 EM, O’Connell PE, et al. 2003. IAHS Decade on Predictions in Ungauged Basins (PUB), 2003–2012: Shaping
872 an exciting future for the hydrological sciences. *Hydrological Sciences Journal* 48 (6): 857–880 DOI:
873 10.1623/hysj.48.6.857.51421
- 874 Sivapalan M. 2009. The secret to ‘doing better hydrological science’: change the question! *Hydrological*
875 *Processes* 23 (9): 1391–1396 DOI: 10.1002/hyp.7242
- 876 Sivapalan M, Blöschl G. 2015. Time scale interactions and the coevolution of humans and water. *Water*
877 *Resources Research* 51 (9): 6988–7022 DOI: 10.1002/2015WR017896



- 878 Soulsby C., Birkel C., Geris J., Dick J., Tunaley, C. and Tetzlaff, D. (2015) Stream water age distributions
879 controlled by storage dynamics and non-linear hydrologic connectivity: modelling with high resolution
880 isotope data. *Water Resources Research*. DOI: 10.1002/2015WR017888
- 881 Soulsby C, Bradford J, Dick J, McNamara JP, Geris J, Lessels J, Blumstock M, Tetzlaff D. 2016. Using
882 geophysical surveys to test tracer-based storage estimates in headwater catchments. *Hydrological
883 Processes* 30 (23): 4434–4445 DOI: 10.1002/hyp.10889
- 884 Sklash MG, Farvolden RN. 1979. The role of groundwater in storm runoff. *Journal of Hydrology* 43 (1): 45–
885 65 DOI: [http://dx.doi.org/10.1016/0022-1694\(79\)90164-1](http://dx.doi.org/10.1016/0022-1694(79)90164-1)
- 886 Tetzlaff, D., Birkel, C., Dick, J., and C. Soulsby (2014) Storage dynamics in hydrogeological units control
887 hillslope connectivity, runoff generation and the evolution of catchment transit time distributions. *Water
888 Resources Research*, DOI: 10.1002/2013WR014147.
- 889 Troch P a., Carrillo G, Sivapalan M, Wagener T, Sawicz K. 2013. Climate-vegetation-soil interactions and
890 long-term hydrologic partitioning: signatures of catchment co-evolution. *Hydrology and Earth System
891 Sciences* 17 (6): 2209–2217 DOI: 10.5194/hess-17-2209-2013
- 892 Van Beek, L.P.H. and M.F.P. Bierkens (2008), The Global Hydrological Model PCR-GLOBWB:
893 Conceptualization, Parameterization and Verification, Report Department of Physical Geography, Utrecht
894 University, Utrecht, The Netherlands, <http://vanbeek.geo.uu.nl/suppinfo/vanbeekbierkens2009.pdf>
- 895 Vrugt J a. 2003. Effective and efficient algorithm for multiobjective optimization of hydrologic models.
896 *Water Resources Research* 39 (8): 1–19 DOI: 10.1029/2002WR001746
- 897 Wang D, Tang Y. 2014. A one-parameter Budyko model for water balance captures emergent behavior in
898 darwinian hydrologic models. *Geophysical Research Letters* 41 (13): 4569–4577
- 899 Wang-Erlandsson L, Bastiaanssen WGM, Gao H, Jägermeyr J, Senay GB, van Dijk AIJM, Guerschman JP,
900 Keys PW, Gordon LJ, Savenije HHG. 2016. Global root zone storage capacity from satellite-based
901 evaporation. *Hydrol. Earth Syst. Sci.* 20 (4): 1459–1481 DOI: 10.5194/hess-20-1459-2016
- 902 Weiler M., McDonnell J. J. 2007 Conceptualizing lateral preferential flow and flow networks and simulating
903 the effects on gauged and ungauged hillslopes. *Water Resour. Res.* 43, W03403
- 904 Ye A, Duan Q, Yuan X, Wood EF, Schaake J. 2014. Hydrologic post-processing of MOPEX streamflow
905 simulations. *Journal of Hydrology* 508: 147–156 DOI: 10.1016/j.jhydrol.2013.10.055



906 Zehe E., Fluehler H. 2001. Preferential transport of Isoproturon at a plot scale and a field scale tile-drained
907 site. J. Hydrol. 247, 100–115

908 Zehe E, Ehret U, Blume T, Kleidon A, Scherer U, Westhoff M. 2013. A thermodynamic approach to link self-
909 organization, preferential flow and rainfall-runoff behaviour. Hydrol. Earth Syst. Sci. 17 (11): 4297–4322
910 DOI: 10.5194/hess-17-4297-2013

911 Zhao R-J, Zuang Y, Fang L, Liu X, Zhang Q. 1980. The Xinanjiang model. Hydrological forecasting —
912 Prévisions hydrologiques 1980 (129): 351–356

913

914

915 Table 1. The parameters of the models, and their prior ranges for calibration. (* S_{uMax} is a parameter in HBV,
916 TOPMODEL and the HSC model, but HSC-MCT model does not have S_{uMax} as a free parameter; ** β is a parameter in
917 HBV model, but not in TOPMODEL, HSC and HSC-MCT models)

Parameter	Explanation	Prior range for calibration
S_{iMax} (mm)	Maximum interception capacity	2
S_{uMax} (mm) *	The root zone storage capacity	(10, 1000)
β (-)**	The shape of the storage capacity curve	(0.01, 5)
C_e (-)	Soil moisture threshold for reduction of evaporation	(0.1, 1)
D (-)	Splitter to fast and slow response reservoirs	(0, 1)
T_{lagF} (d)	Lag time from rainfall to peak flow	(0, 10)
K_f (d)	The fast recession coefficient	(1, 20)
K_s (d)	The slow recession coefficient	(20, 400)

918

919

920 Table 2. The water balance and constitutive equations used in models. (Function (15)[†] is used in the HBV model, but
921 not used in the TOPMODEL, HSC and HSC-MCT models)

reservoirs	Water balance equations	Constitutive equations
------------	-------------------------	------------------------



Interception
reservoir

$$\frac{dS_i}{dt} = P - E_i - P_e \quad (8)$$

$$E_i = \begin{cases} E_p; S_i > 0 \\ 0; S_i = 0 \end{cases} \quad (9)$$

$$P_e = \begin{cases} 0; S_i < S_{iMax} \\ P; S_i = S_{iMax} \end{cases} \quad (10)$$

Unsaturated
reservoir

$$\frac{dS_u}{dt} = P_e - E_a - R_u \quad (11)$$

$$\frac{R_u}{P_e} = \left(\frac{S_u}{S_{uMax}} \right)^\beta \quad (12)^*$$

$$\frac{E_a}{E_p - E_i} = \frac{S_u}{C_e S_{uMax}} \quad (13)$$

Splitter and
Lag function

$$R_f = R_u D \quad (17); \quad R_s = R_u (1 - D) \quad (14)$$

$$R_f(t) = \sum_{i=1}^{T_{lagf}} c_f(i) \cdot R_f(t - i + 1) \quad (15)$$

$$c_f(i) = i / \sum_{u=1}^{T_{lagf}} u \quad (16)$$

Fast reservoir

$$\frac{dS_f}{dt} = R_f - Q_f \quad (17)$$

$$Q_f = S_f / K_f \quad (18)$$

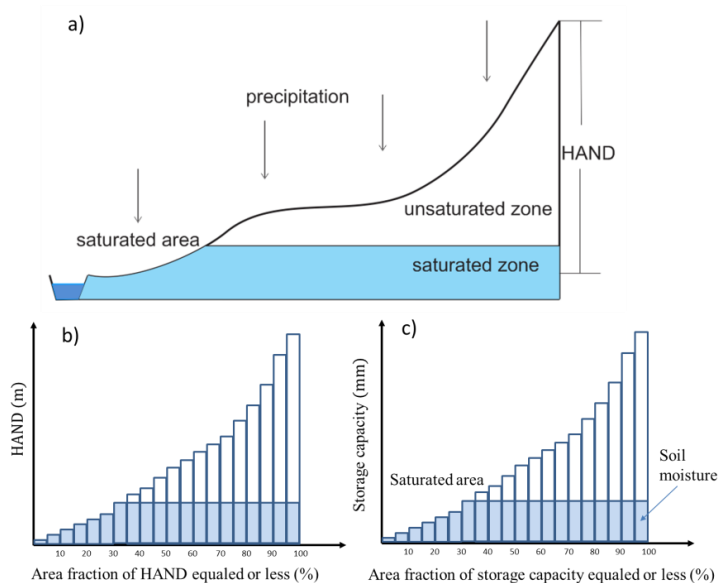
Slow reservoir

$$\frac{dS_s}{dt} = R_s - Q_s \quad (19)$$

$$Q_s = S_s / K_s \quad (20)$$

922

923

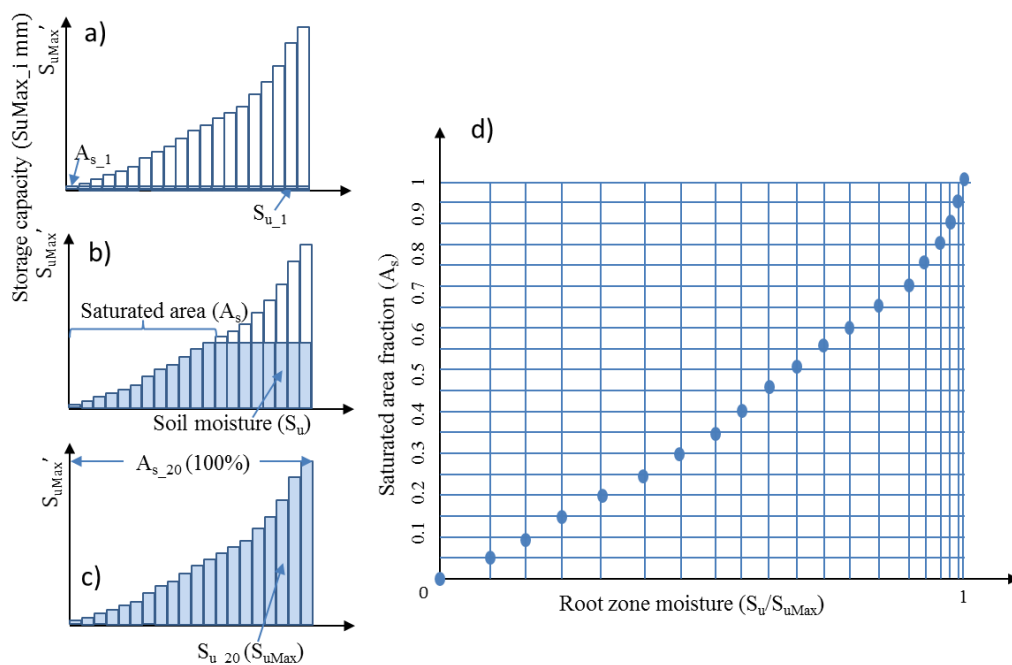


924

925 Figure 1. The perceptual model of the HAND-based Storage Capacity curve (HSC) model. a) shows the representative
 926 hillslope profile in nature, and the saturated area, unsaturated zone and saturated zone; b) shows the relationship
 927 between HAND bands and their corresponded area fraction; c) shows the relationship between storage capacity-
 928 area fraction-soil moisture-saturated area, based on the assumption that storage capacity linearly increases with
 929 HAND values.

930

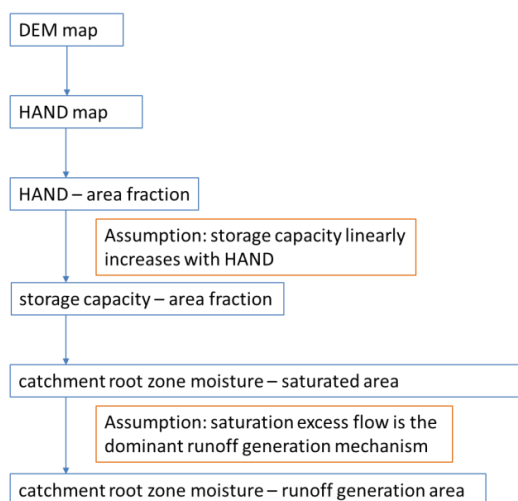
931



932

933 Figure 2. The conceptual model of the HSC model. a), b) and c) illustrate the relationship between soil moisture (S_u)
 934 and saturated area (A_s) in different soil moisture conditions. In d), 20 different S_u - A_s conditions are plotted, which
 935 allow us to estimate A_s from S_u .

936

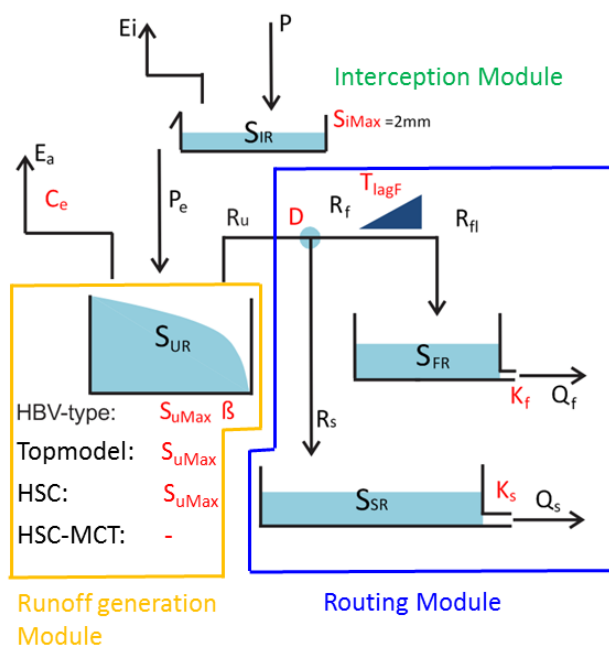


937

938 Figure 3. The procedures estimating runoff generation by the HSC model and its two hypotheses.



939

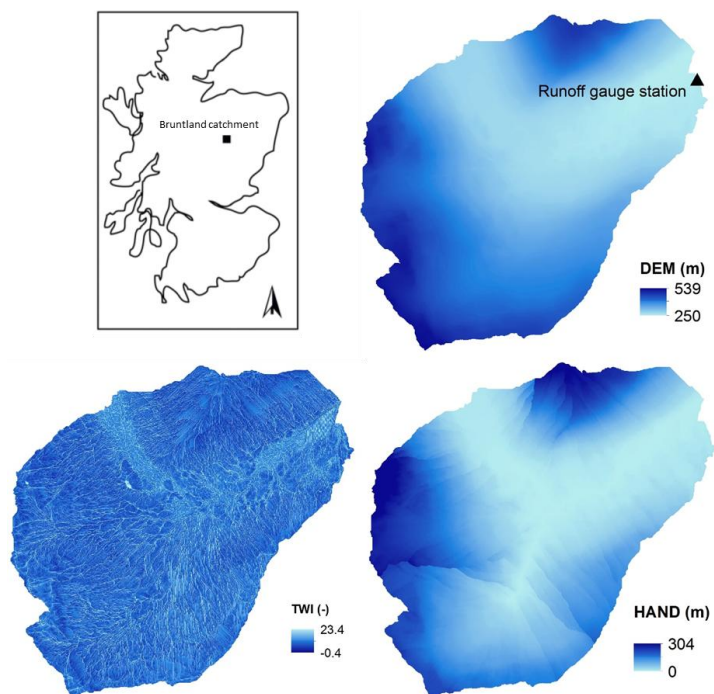


940

941 Figure 4. Model structure and free parameters, involving four runoff generation models (HBV-type, TOPMODEL, HSC,
 942 and HSC -MCT). HBV-type has S_{uMax} and beta two free parameters; TOPMODEL and HSC models have S_{uMax} as one
 943 free parameter; and HSC-MCT model does not have free parameter. In order to simplify calibration process and
 944 make fair comparison, the interception storage capacity (S_{iMax}) was fixed as 2mm.

945

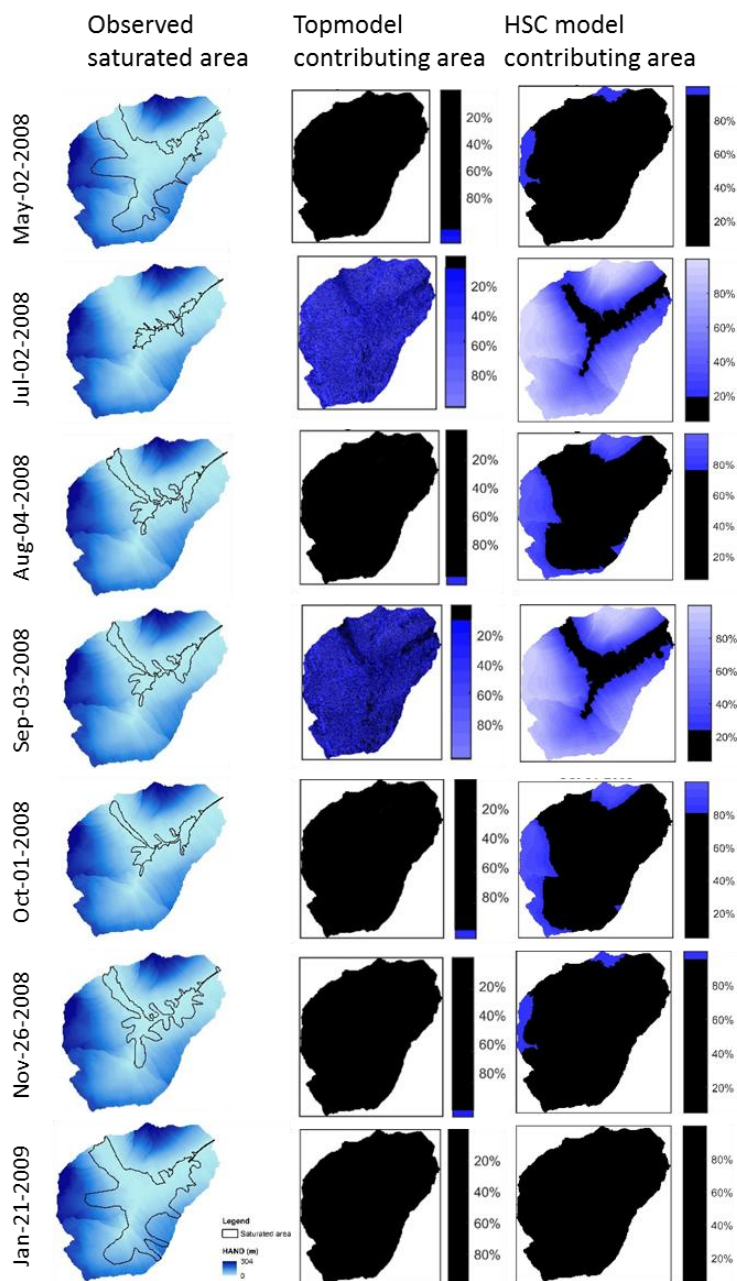
946



947

948 Figure 5. (a) Study site location of the Bruntland Burn catchment within Scotland; (b) digital elevation model (DEM)
949 of the Bruntland Burn catchment; (c) the topographic wetness index map of the Bruntland Burn catchment; (d) the
950 height above the nearest drainage (HAND) map of the Bruntland Burn catchment.

951

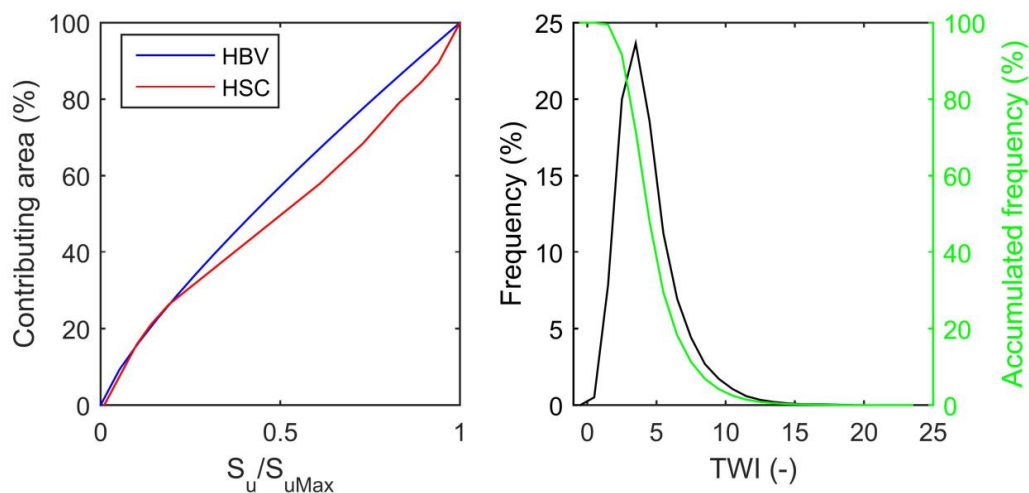


952

953 Figure 6. The measured saturated areas and the simulated contributing areas by TOPMODEL and HSC models.

954

955

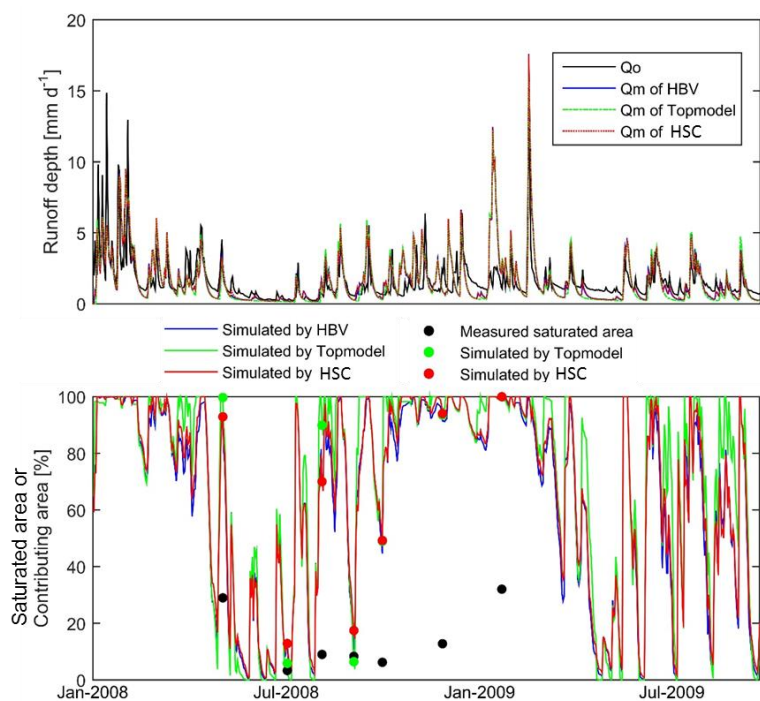


956

957 Figure 7. The curves of the beta function of HBV model, and the S_u - A_s curve generated by HSC model (the left figure).

958 The frequency and accumulated frequency of the TWI in the Bruntland Burn catchment (the right figure).

959



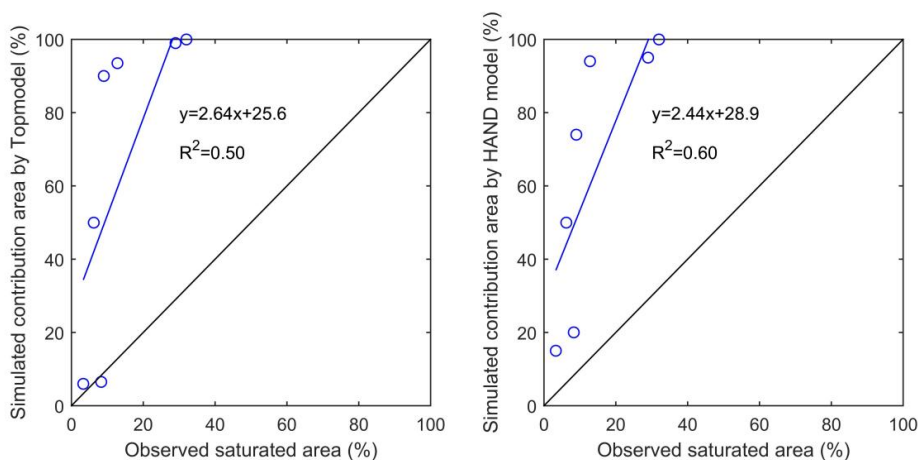
960



961 Figure 8. The observed hydrograph (Q_o , black line) of the Bruntland Burn catchment in 2008. And the simulated
962 hydrographs (Q_m) by HBV model (blue line), TOPMODEL (green dash line), HSC model (red dash line). And the
963 comparison of the simulated relative soil moistures, i.e. HBV (blue line), TOPMODEL (green line), HSC (red line). And
964 the observed saturated area of 7 days (black dots), and the correspondent simulated contributing area by
965 TOPMODEL (green dots) and by HSC model (red dots).

966

967



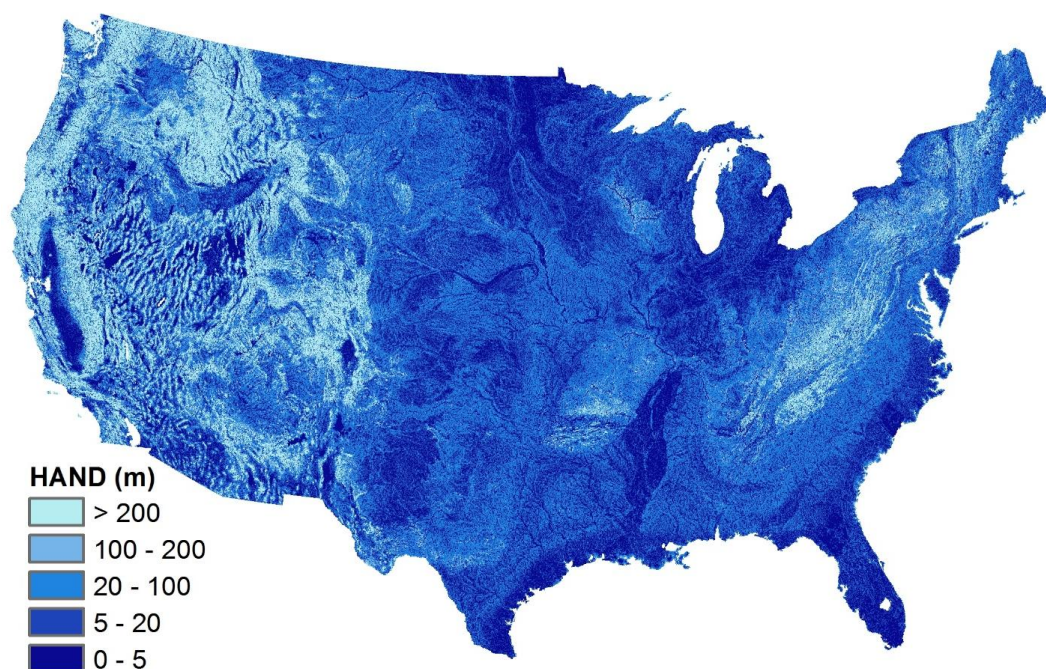
968

969 Figure 9. The comparison of the observed saturated area and simulated contributing areas by TOPMODEL and HSC
970 models.

971

972

973

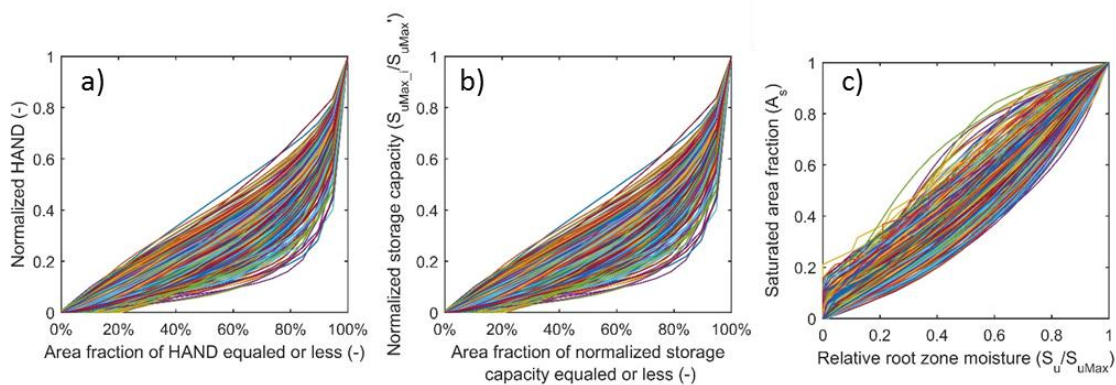


974

975 Figure 10. The Height Above the Nearest Drainage (HAND) map of the CONUS.

976

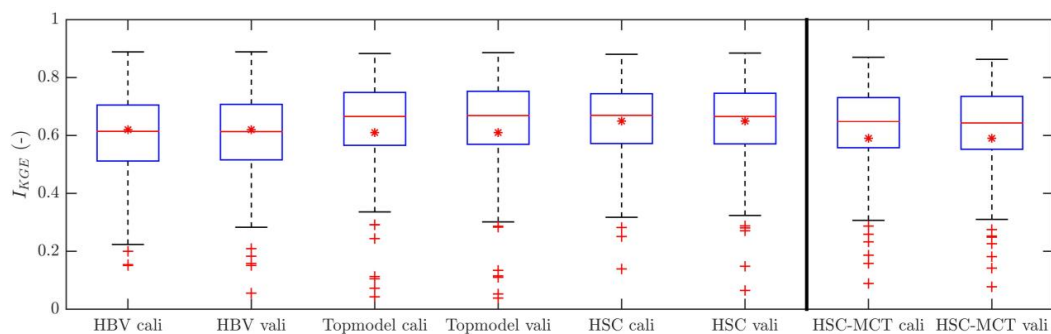
977



978

979 Figure 11. a) The profiles of the normalized HAND of the 323 MOPEX catchments; b) the relations between area
 980 fraction and the normalized storage capacity profile of the 323 MOPEX catchments; c) the S_u - A_s curves of the HSC
 981 model which can be applied to estimate runoff generation from relative soil moisture for the 323 MOPEX catchment.

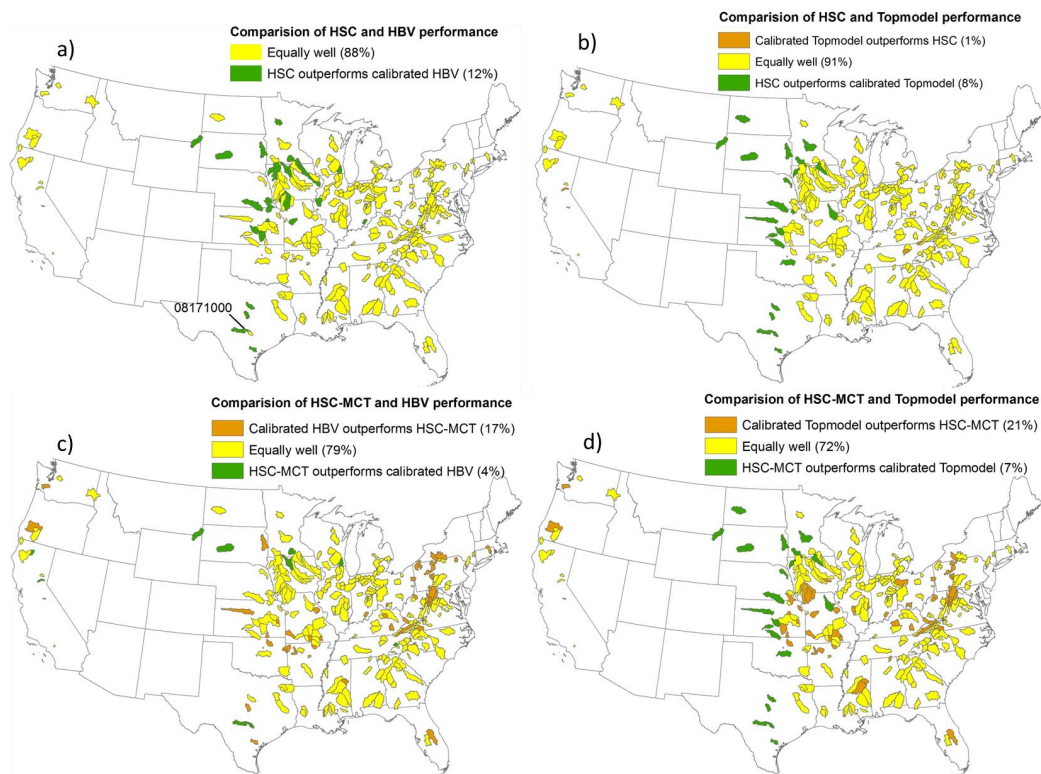
982



983

984 Figure 12. The comparison between the HBV, the TOPMODEL, the HSC, and the HSC-MCT models

985



986

987 Figure 13. Performance comparison of the HSC and HSC-MCT models compared to two benchmark models: HBV
 988 and TOPMODEL, for the 323 MOPEX catchments.